

A single-cell mathematical model of SARS-CoV-2 induced pyroptosis and the effects of anti-inflammatory intervention

Sara J Hamis,¹  Fiona R Macfarlane,¹ 

1 School of Mathematics and Statistics, University of St Andrews, St Andrews, Scotland, UK.

 Both authors contributed equally to this work.

This is version 2 of the pre-print article.

Abstract

Pyroptosis is an inflammatory mode of cell death that can contribute to the cytokine storm associated with severe cases of coronavirus disease 2019 (COVID-19). The formation of the NLRP3 inflammasome is central to pyroptosis, which may be induced by severe acute respiratory syndrome coronavirus 2 (SARS-CoV-2). Inflammasome formation, and by extension pyroptosis, may be inhibited by certain anti-inflammatory drugs. In this study, we present a single-cell mathematical model that captures the formation of the NLRP3 inflammasome, pyroptotic cell death and responses to anti-inflammatory intervention that hinder the formation of the NLRP3 inflammasome. The model is formulated in terms of a system of ordinary differential equations (ODEs) that describe the dynamics of the biological components involved in pyroptosis. Our results demonstrate that an anti-inflammatory drug can delay the formation of the NLRP3 inflammasome, and thus may alter the mode of cell death from inflammatory (pyroptosis) to non-inflammatory (e.g., apoptosis). The single-cell model is being implemented in a SARS-CoV-2 Tissue Simulator, in collaboration with a multidisciplinary coalition investigating within host-dynamics of COVID-19. In this paper, we provide an overview of the SARS-CoV-2 Tissue Simulator and highlight the effects of pyroptosis on a cellular level.

1 Introduction

1.1 SARS-CoV-2 induced pyroptosis and cytokine storms

COVID-19 is a respiratory illness induced by the coronavirus strain SARS-CoV-2 [1]. Most people infected by the virus experience mild symptoms, however, in severe cases of the disease, life-threatening symptoms can manifest [2]. These divergent disease trajectories have been, largely, attributed to differences in the immune response of infected hosts [3]. When cells register the presence of SARS-CoV-2 virions, a multitude of host-protective responses are triggered. Infected cells transmit signals that recruit immune cells, such as monocytes, macrophages and T-cells, to the site of infection. These immune cells act to eliminate the virus from the body, and thus they attack infected cells in which virions may replicate. Current research has shown that, upon active virion replication and release, SARS-CoV-2 can induce pyroptosis in both epithelial cells and immune cells [3–9]. Pyroptosis is an inflammatory and rapid mode of cell death that is characterised by the secretion of pro-inflammatory cytokines, cell swelling and, ultimately, membrane rupture resulting in the release of cytoplasmic contents into the extracellular environment [10, 11]. Furthermore, interleukin-1 β (IL-1 β), a cytokine released by pyroptosing cells, has been shown to induce pyroptosis in neighbouring bystander cells [12]. Fundamentally, both the recruitment of immune cells and pyroptotic cell death act to protect the host from the virus. Indeed, in hosts with healthy immune systems, virus-specific T-cells are recruited to the site of infection [3], and cytokine levels are kept under control by negative feedback regulations [13]. However, if the immune system contesting a viral infection is malfunctioning, a wide array of cytokines may be over-produced due to deregulation of the negative feedback that controls cytokine levels in healthy immune systems [13]. Such an over-compensating immune response may lead to uncontrolled cytokine activity, commonly referred to as a *cytokine storm* [3]. Elevated levels of both pro-inflammatory and anti-inflammatory cytokines have been observed in severe cases of COVID-19 [2, 9, 13, 14], commonly manifesting

with severe symptoms such as pneumonia and acute respiratory distress syndrome (ARDS), which may lead to multiple organ failure [13]. Hence, cytokine storms are associated with poor clinical COVID-19 outcomes [2, 4, 6]. Therefore, suppressing the onset of cytokine storms and the subsequent inflammation, without completely cancelling-out host-protective effects of the immune system, is one of the suggested treatment strategies being explored to combat COVID-19 [13]. One approach to suppress cytokine storms is to inhibit pyroptosis whilst leaving other functionalities of the immune system untouched. In fact, there exists a number of anti-inflammatory drugs that may inhibit pyroptosis and, through the inhibition of pyroptosis, alter the mode of cell death from inflammatory to non-inflammatory [15]. Non-inflammatory modes of cell death includes apoptosis, which is characterised by cell shrinkage with cell membrane integrity maintained throughout cell death, whereas pyroptosis is characterised by cell swelling and membrane rupture [16, 17]. Inhibiting pyroptosis may provide two key clinical advantages. Firstly, this inhibition could suppress the cytokine storm, and the resulting increased inflammation and tissue damage that it brings. Secondly, it has been shown that tissue factors released upon pyroptosis may initiate blood coagulation cascades, therefore inhibiting pyroptosis may reduce the risk of blood clotting in COVID-19 cases [2].

1.2 The pathway to pyroptosis

In this subsection we describe key aspects of the intracellular pathway that leads to pyroptosis. For a more comprehensive description of the mechanisms driving pyroptosis, we refer the interested reader to detailed reviews [15, 18–21]. Using the details from a well-established biological pathway of pyroptosis, we formulate a mathematical model described in Section 2, the components of the model are illustrated in Figure 1.

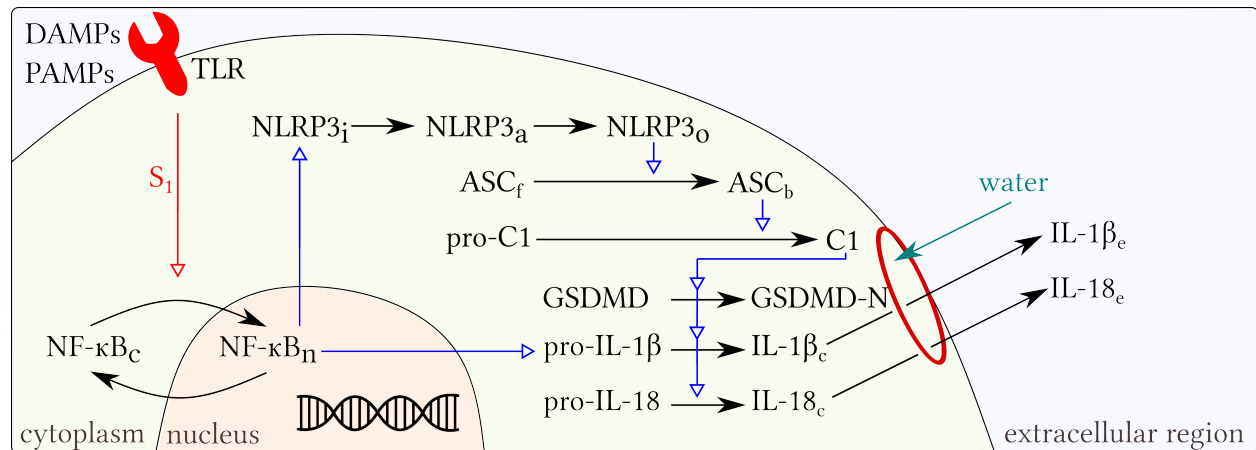


Figure 1. A schematic representation of the pathway to pyroptosis, as considered in our mathematical model. Black arrows represent reactions that involve mass transfer between depicted compounds. Blue arrows represent facilitation of compound formation or reactions. Red arrows represent signals that can be turned *on* or *off* in the model. Membrane pores (shown in red) induced by GSDMD-N allows for the outflux of inflammatory cytokines and the influx of extracellular water, causing the cell to swell and the cell membrane to eventually rupture. Abbreviations are listed in Appendix A.

Central to pyroptosis is the formation of the inflammasome, a multi-protein complex consisting of three molecular units (a sensor, an adaptor and an executor) that together enable the release of cytokines and the ultimate membrane rupture that characterise pyroptosis. This inflammasome is named after its sensor molecule NLRP3, *i.e.*, nucleotide-binding and oligomerisation domain (NBD) leucine-rich repeat (LRR)-containing receptors with an N-terminal pyrin domain (PYD) 3. Thus in this study we focus our attention on the inflammasome comprising the sensor molecule NLRP3, the adaptor molecule apoptosis-associated speck-like protein (ASC), and the executor molecule caspase-1. Note that, only one inflammasome is formed per cell [19].

Homeostatic cells do not contain enough NLRP3 to produce an inflammasome base [20], instead, NLRP3 levels are elevated in cells when toll like receptors (TLRs) on the cell surface sense DAMPs or pathogen associated molecular patterns (PAMPs). As SARS-CoV-2 is a positive sense RNA virus, it can indeed be detected by TLRs and induce NLRP3 inflammasome formation [2, 6, 7]. Upon TLRs detecting DAMPs or PAMPs, the transcription factor NF- κ B is translocated to the nucleus, initiating the transcription and, by extension, the synthesis of (inactive) NLRP3. The transcription and synthesis of the pro-inflammatory cytokine pro-interleukin-1 β (pro-IL-1 β) is also regulated by NF- κ B. The transcription-mediated elevation of (inactive) NLRP3 and pro-IL-1 β is often referred to as the *priming* step of pyroptosis, which is succeeded by the *activation* step [19].

Inactive NLRP3 can become activated upon stimuli from a wide array intracellular events, including altered calcium signalling, potassium efflux and the generation of reactive oxygen species (ROS) [15]. In turn, active NLRP3 molecules can oligomerise and bind together to form a wheel shaped structure, constituting the inflammasome base as depicted in Figure 2(a). Through homotypic binding, ASC molecules can then bind to the NLRP3 inflammasome base as depicted in Figure 2(b). Thereafter, pro-caspase-1 can bind to ASC, enabling the proximity-induced dimerisation, and thereby the activation, of caspase-1 [22]. Active caspase-1 then acts to cleave the pro-interleukins, pro-IL-1 β and pro-IL-18, into their respective mature forms, IL-1 β and IL-18. Caspase-1 also cleaves the protein gasdermin D (GSDMD), releasing the active N-terminal domain of gasdermin D (GSDMD-N) which can form pores on the cell membrane. These pores enable the *outflux* of the inflammatory cytokines IL-1 β and IL-18 (in their mature forms) from the cytoplasm to the external environment [23, 24]. The released cytokines can recruit immune cells to the site of infection and initiate pyroptosis in neighbouring cells. Furthermore, the GSDMD-N derived membrane pores also allow for the *influx* of extracellular material, *e.g.*, water, into the cell. This influx causes cells to swell until their plasma membrane eventually ruptures, releasing cellular material into the extracellular region.

Data suggests that ASC, pro-caspase-1, GSDMD and pro-IL-18 are present in adequate levels for NLRP3 formation and pyroptosis at homeostasis, and thus these proteins are not upregulated by the TLR-stimulated cytoplasm-to-nucleus translocation of NF- κ B [18, 25]. Furthermore, once the NLRP3 inflammasome is activated, cell lysis can be delayed but not prevented [26, 27]. However, if the formation of the NLRP3 inflammasome is inhibited, a series of intracellular events resulting in non-inflammatory cell death may instead be initiated. There exists multiple drugs that act to inhibit inflammasome formation in order to prevent pyroptosis, a rigorous list of covalent drugs that target the NLRP3 inflammasome can be found in a review by Bertinara *et al.* [15]. In this study, we include the pharmacodynamical effects of a generic anti-inflammatory drug which inhibits the formation of the NLRP3 inflammasome by covalently binding to NLRP3 molecules to prevent NLRP3-NLRP3 interactions, as shown in Figure 2(a).

1.3 Mathematical modelling of pyroptosis

The use of mathematical models to describe apoptotic cell death has been well established and reviewed [28, 29]. However, there are significantly fewer mathematical models that describe pyroptotic cell death. Previous modelling works include more implicit descriptions of pyroptosis [30] and descriptions of specific aspects of inflammasome formation [31–33]. Within this work, we explicitly model the intracellular events that drive SARS-CoV-2 induced pyroptosis, from TLRs detecting DAMPs/PAMPs through to the ultimate membrane rupture. We study this system in the absence, or presence, of an anti-inflammatory drug. The goal of our model is to capture key aspects of the pyroptosis pathway that are commonly analysed in experimental studies. Thus, in this mathematical/computational work, we study the time evolution of NF- κ B, the NLRP3 inflammasome and its components, the pore-forming protein GSDMD, the pro-inflammatory cytokines IL-1 β and IL-18, and cell volume.

1.4 Mathematical modelling of within host-dynamics of COVID-19

Many researchers have turned their attention to the mathematical modelling of COVID-19 since the virus was announced as a global pandemic [34]. These models are split into two main categories, which are, external dynamics, (*e.g.*, models of the spread of COVID-19 from person to person), and modelling of the within-host dynamics of COVID-19. We shall focus on the latter, where the spread of the virus is described

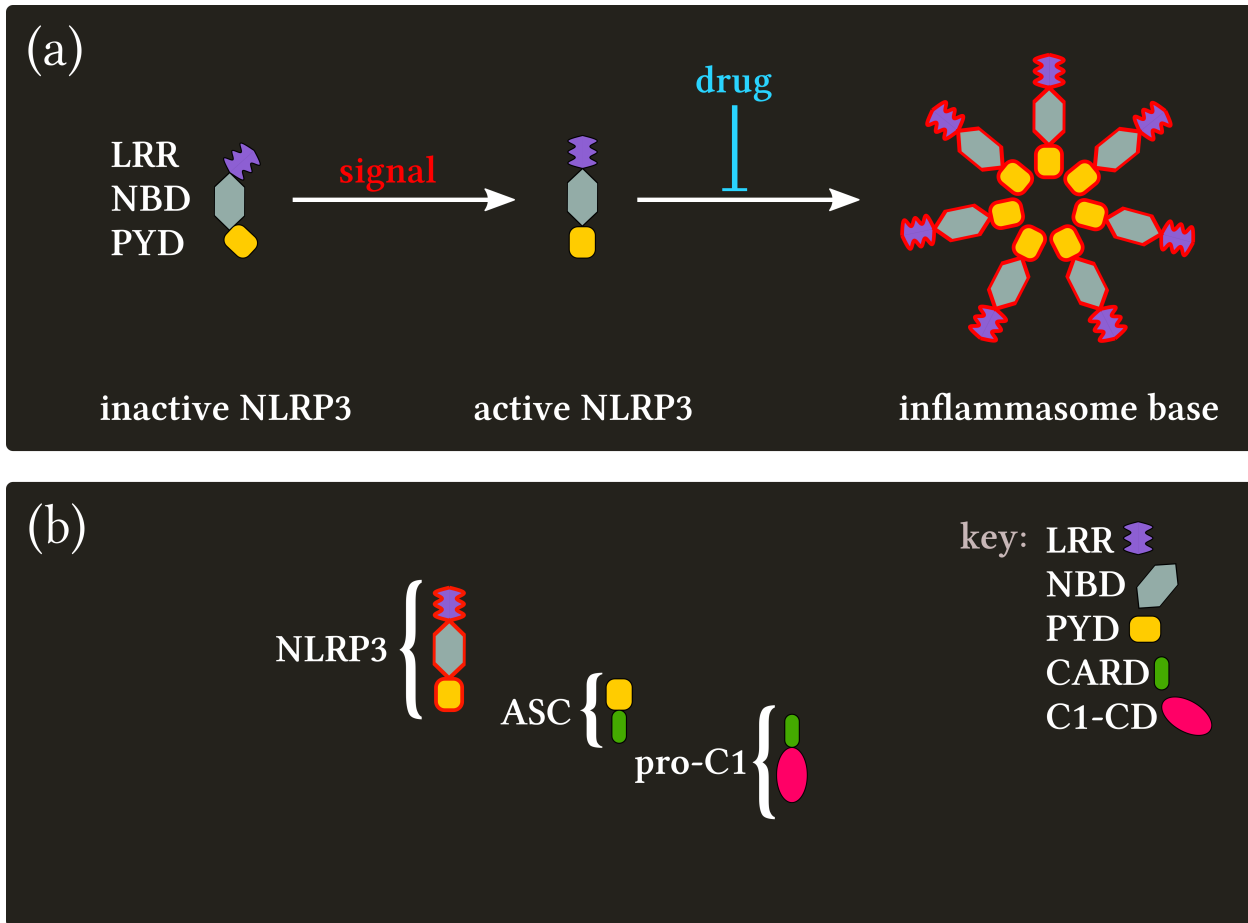


Figure 2. NLRP3 inflammasome formation. (a) Through a wide array of stimuli, inactive NLRP3 can become activated. Active NLRP3 can bind together to form the inflammasome base, this binding may be inhibited by NLRP3-targeting anti-inflammatory drugs. (b) Once the inflammasome base is formed, the pyrin domain (PYD) of ASC molecules can bind to the PYD of NLRP3 molecules in the inflammasome base. Thereafter, the caspase activation and recruitment domain (CARD) of pro-caspase-1 can bind to the CARD of NLRP3-bound ASC molecules. This results in the dimerisation and activation of caspase-1. Abbreviations used in the figure are listed in Appendix A.

within the body. Agent-based models (ABMs) have been widely utilised in the past to model within-host viral dynamics [35–38], with focuses on influenza modelling [39–43], oncolytic virotherapy [44, 45] and inflammation [46, 47]. Several groups are utilising multiscale ABMs to describe these within-host dynamics of SARS-CoV-2 [48–50]. These modelling approaches aim to describe how the virus spreads within the body and circumvents the human immune system. Our model of single-cell inflammatory cell death is being incorporated within a multiscale SARS-CoV-2 tissue simulator set up as part of an international, multidisciplinary coalition. For the full details of this agent-based model, we refer the reader to the preprint for the project [50]. Here, we will focus on the role of pyroptosis in the tissue simulator, as described in Section 3.

2 Mathematical model of pyroptosis in a single-cell

We formulate a system of ordinary differential equations (ODEs) describing the dynamics of the key components of NLRP3 inflammasome formation and pyroptosis. Specifically, the model includes the dynamics of NF- κ B (Section 2.1), NLRP3 (Section 2.2), ASC (Section 2.3), caspase-1 (Section 2.4), GSDMD (Section 2.5), IL-1 β and IL-18 (Section 2.6). We also consider changes in cell volume over time (Section 2.7). Figure 1 provides a pictorial overview of the modelled pathway, while variable names are listed in Table B.1 and, throughout this work, the bracket notation [] denotes compound concentration. Further details concerning modelling choices and parameterisation can be found in Appendices B and C, respectively. In Section 2.8, we expand the model to include the pharmacodynamic effects of an anti-inflammatory drug targeting NLRP3. We discuss the results of numerical simulations of the model in Section 2.10, and further investigate the model using sensitivity analysis in Section 2.11.

2.1 NF- κ B dynamics

When TLRs register DAMPs or PAMPs, cytoplasmic NF- κ B is translocated to the nucleus in order to initiate the transcription of inactive NLRP3 and pro-IL-1 β . In the case of SARS-CoV-2, for example, these DAMPs and PAMPs can be induced by intracellular virion replication and release, or by cytokines from neighbouring, infected cells. Dynamics of NF- κ B translocation between the cytoplasm and the nucleus varies between situations and strongly depends on cell type or external stimuli [51]. In recent work, Bagaev *et al.* [51] studied TLR-4 derived activation of NF- κ B in bone marrow derived macrophages (BMDMs) subjected to bacterial lipopolysaccharide (LPS). The authors found a sharp peak in NF- κ B nuclear translocation kinetics 10 minutes post LPS activation, after which the nuclear NF- κ B signalling gradually decreased until plateau. As BMDMs stimulated with LPS have been shown to undergo pyroptosis [52, 53], we here aim to capture these rapid, mono-peaking and right-skewed nuclear NF- κ B dynamics. In our model we therefore assume that the signal S_1 initiates a rapid cytoplasm-to-nucleus translocation of NF- κ B, and that the nuclear occupancy of NF- κ B over time follows a log-normal probability distribution function. Thus, when S_1 is activated, the concentration of nuclear NF- κ B, $[NF\kappa B_n]$, can be estimated using

$$[NF\kappa B_n](\bar{t}) = C \cdot \frac{1}{\bar{t}\sigma\sqrt{2\pi}} e^{-\frac{\log^2 \bar{t}}{2\sigma^2}}, \quad (1)$$

where C is a constant (in units of concentration) and t is chosen to be the time in minutes and $\bar{t} = t/\tau$, for a constant τ (in units of minutes). Substituting variables $s = 2\sigma^2$ and $\nu = C^{-1}\tau^{-1}\sigma\sqrt{2\pi}$ we obtain

$$[NF\kappa B_n](\bar{t}) = \frac{\tau}{t\nu} e^{-\frac{\log^2 \bar{t}}{s}}. \quad (2)$$

By differentiation, with respect to time, of Equation (2), the amount of nuclear NF- κ B ($[NF\kappa B_n]$) over time can thus be approximated using an ordinary differential equation,

$$\frac{d[NF\kappa B_n]}{dt} = \frac{d[NF\kappa B_n]}{d\bar{t}} \frac{d\bar{t}}{dt} = \frac{d[NF\kappa B_n]}{d\bar{t}} \frac{1}{\tau} = -S_1 \cdot \frac{1}{\bar{t}^2 s \nu} (2 \log(\bar{t}) + s) e^{-\frac{\log^2 \bar{t}}{s}}, \quad (3)$$

where the DAMP/PAMP initiated TLR-signal S_1 has been explicitly included as a binary *on/off* function such that

$$S_1 := \begin{cases} 1 & \text{on, if a DAMP/PAMP induced signal is present,} \\ 0 & \text{off, otherwise.} \end{cases} \quad (4)$$

The parameters τ , s and ν can be varied to adjust the height, width and skewness of the NF- κ B peak.

2.2 NLRP3 dynamics

Following nuclear NF- κ B translocation, inactive NLRP3, NLRP3_i , is transcribed and subsequently synthesised. As the transcription and synthesis of inactive NLRP3 is promoted by nuclear NF- κ B, we describe the production rate of NLRP3 using a Hill function. Specifically, a Hill function [54] with a constant coefficient rate α_1 , Hill coefficient γ_{NF} and half-max concentration-value NF_{50} . Inactive NLRP3 can become activated in response to a secondary signal, S_2 , which can be turned *on* by multiple stimuli such as potassium influx, calcium outflux and abnormal reactive oxygen species (ROS). Once activated, NLRP3_a molecules can oligomerise (bind together) to form a wheel-shaped inflammasome base, modelled by the concentration of oligomerised NLRP3, *i.e.*, NLRP3_o . In the model, we thus consider NLRP3 protein concentrations in three different forms: $[\text{NLRP3}_i]$, $[\text{NLRP3}_a]$ and $[\text{NLRP3}_o]$. Inactive and active NLRP3 decays in the model at a rate δ_1 . Note, we do not consider the decay of NLRP3_o as we assume the inflammasome will remain formed until pyroptosis has completed. The forward reactions from the inactive-to-active, and active-to-oligomerised NLRP3 forms are here assumed to be irreversible, and are respectively described using the rates k_2 and k_3 . We now incorporate all the above mechanisms to describe the rate of change of $[\text{NLRP3}_i]$, $[\text{NLRP3}_a]$ and $[\text{NLRP3}_o]$ over time as,

$$\frac{d[\text{NLRP3}_i]}{dt} = \alpha_1 \frac{[\text{NF-}\kappa\text{B}_n]^{\gamma_{\text{NF}}}}{\text{NF}_{50}^{\gamma_{\text{NF}}} + [\text{NF-}\kappa\text{B}_n]^{\gamma_{\text{NF}}}} - S_2 k_2 [\text{NLRP3}_i] - \delta_1 [\text{NLRP3}_i], \quad (5)$$

$$\frac{d[\text{NLRP3}_a]}{dt} = S_2 k_2 [\text{NLRP3}_i] - k_3 [\text{NLRP3}_a] - \delta_1 [\text{NLRP3}_a], \quad (6)$$

$$\frac{d[\text{NLRP3}_o]}{dt} = k_3 [\text{NLRP3}_a], \quad (7)$$

where $[\overline{\text{NF-}\kappa\text{B}_n}]$ denotes the deviation from baseline in $[\text{NF-}\kappa\text{B}_n]$ so that

$$[\overline{\text{NF-}\kappa\text{B}_n}](t) = [\text{NF-}\kappa\text{B}_n](t) - [\text{NF-}\kappa\text{B}_n](0). \quad (8)$$

The binary signal S_2 is set as

$$S_2 := \begin{cases} 1 & \text{on, if secondary activation signal is present,} \\ 0 & \text{off, otherwise.} \end{cases} \quad (9)$$

2.3 ASC dynamics

Once the inflammasome base is formed, free ASC in the cell can bind to the NLRP3 inflammasome base. Thus in the model, we consider the concentrations of ASC in free and bound form, denoted $[\text{ASC}_f]$ and $[\text{ASC}_b]$, respectively. The inflammasome-forming binding is here considered to be irreversible and occurs at a rate k_4 , hence the rate of change of $[\text{ASC}_f]$ and $[\text{ASC}_b]$ are here described by

$$\frac{d[\text{ASC}_f]}{dt} = -k_4 F([\text{NLRP3}_o]) [\text{NLRP3}_o] [\text{ASC}_f], \quad (10)$$

$$\frac{d[\text{ASC}_b]}{dt} = k_4 F([\text{NLRP3}_o]) [\text{NLRP3}_o] [\text{ASC}_f], \quad (11)$$

where the function $F([\text{NLRP3}_o])$ is included in order to model the absence or presence of the NLRP3 inflammasome base. In order to allow for more mathematical analyses, we approximate this two-state system as a continuous sigmoid function [55] such that

$$F([\text{NLRP3}_o]) = \frac{1}{1 + \left(\frac{[\text{NLRP3}_o] + a}{b}\right)^{-c}} \quad (12)$$

where values $a = 1$ (a.u.) and $b = 2$ (a.u.) can be used to obtain $F([\text{NLRP3}_o]) \approx 0$ for $[\text{NLRP3}_o] < 1$ and $F([\text{NLRP3}_o]) \approx 1$ otherwise. The value of c is set to be large (*e.g.*, 1000) in order to create a steep curve in the sigmoid. Note that, free ASC levels are adequate for pyroptosis at homeostasis [15,18], and thus the total amount of ASC is conserved in our model,

$$[\text{ASC}_f] + [\text{ASC}_b] = \text{constant}. \quad (13)$$

2.4 Caspase-1 dynamics

Pro-caspase-1 can bind to inflammasome-bound ASC upon availability and subsequently dimerise into its activated, mature form, caspase-1. In our model, concentrations of pro-caspase-1 and caspase-1 are denoted by $[\text{pro-C1}]$ and $[\text{C1}]$, respectively. Caspase-1 activation occurs at a rate k_5 and is here assumed to be irreversible so that the rate of change of $[\text{pro-C1}]$ and $[\text{C1}]$ can be described by

$$\frac{d[\text{pro-C1}]}{dt} = -k_5 [\text{ASC}_b] [\text{pro-C1}], \quad (14)$$

$$\frac{d[\text{C1}]}{dt} = k_5 [\text{ASC}_b] [\text{pro-C1}]. \quad (15)$$

Pro-caspase-1 is present in adequate levels in the cell prior to cellular responses to DAMPs or PAMPs [15,18], therefore the total amount of caspase-1, in both pro- and active form, is conserved over time so that

$$[\text{pro-C1}] + [\text{C1}] = \text{constant}. \quad (16)$$

2.5 Gasdermin dynamics

GSDMD-N, which is formed as a result of caspase-1 cleavage of GSDMD, produces pores on the cell membrane that are central to the pyroptosis process. In the model, we consider the concentrations of both GSDMD and GSDMD-N, denoted as $[\text{GSDMD}]$ and $[\text{GSDMD-N}]$, respectively. We describe the caspase-1 facilitated cleavage using a Hill function, where γ_{C1} is the Hill coefficient, and C_{150} is the half-max $[\text{C1}]$ value. We additionally assume a specific rate for $[\text{GSDMD}]$ cleavage, α_2 . Therefore, we describe the rate of change of $[\text{GSDMD}]$ and $[\text{GSDMD-N}]$ in the model, through the equations,

$$\frac{d[\text{GSDMD}]}{dt} = -\alpha_2 \frac{[\text{C1}]^{\gamma_{C1}}}{C_{150}^{\gamma_{C1}} + [\text{C1}]^{\gamma_{C1}}} [\text{GSDMD}], \quad (17)$$

$$\frac{d[\text{GSDMD-N}]}{dt} = \alpha_2 \frac{[\text{C1}]^{\gamma_{C1}}}{C_{150}^{\gamma_{C1}} + [\text{C1}]^{\gamma_{C1}}} [\text{GSDMD}]. \quad (18)$$

Adequate levels of GSDMD required for pyroptosis are available in the cell at homeostasis [25], therefore we include a conservation law,

$$[\text{GSDMD}] + [\text{GSDMD-N}] = \text{constant}. \quad (19)$$

2.6 Cytokine dynamics

Translocation of NF- κ B, from the cytoplasm to the nucleus, induces the transcription and synthesis of pro-IL-1 β . Pro-IL-18, on the other hand, is present in adequate levels within the cell, therefore we not consider synthesis. When active caspase-1 is available, the pro-forms of the interleukins can be cleaved into their activated forms. Subsequently, once membrane pores have been formed in response to GSDMD-N activity, cytoplasmic interleukins may be secreted into the extracellular region. We here consider the concentrations of IL-1 β /18 in pro-, cytoplasmic and extracellular form, respectively denoted [pro-IL-1 β /18], [IL-1 β _c/18_c] and [IL-1 β _e/18_e]. In the model, pro-IL-1 β and pro-IL-18 are cleaved by caspase-1 at rates α_4 and α_5 , respectively. Once cleaved, cellular IL-1 β _c and IL-18_c are secreted through the GSDMD-N derived pores at the rates k_6 and k_7 , respectively.

IL-1 β : The transcription and synthesis of pro-IL-1 β is promoted by $[\text{NF-}\kappa\text{B}_n]$, in a similar way to NLRP3, therefore we describe this process using a Hill function with constant coefficient α_3 , Hill coefficient γ_{NF} and the half-max concentration of NF- κ B, NF_{50} . We additionally consider the decay of IL-1 β at the rate δ_2 . We incorporate the above mechanisms to describe the rate of change of [pro-IL-1 β], [IL-1 β _c] and [IL-1 β _e] over time as,

$$\frac{d[\text{pro-IL-1}\beta]}{dt} = \alpha_3 \frac{[\text{NF-}\kappa\text{B}_n]^{\gamma_{\text{NF}}}}{\text{NF}_{50}^{\gamma_{\text{NF}}} + [\text{NF-}\kappa\text{B}_n]^{\gamma_{\text{NF}}}} - \alpha_4 \frac{[\text{C1}]^{\gamma_{\text{C1}}}}{\text{C1}_{50}^{\gamma_{\text{C1}}} + [\text{C1}]^{\gamma_{\text{C1}}}} [\text{pro-IL-1}\beta] - \delta_2 [\text{pro-IL-1}\beta], \quad (20)$$

$$\frac{d[\text{IL-1}\beta_c]}{dt} = \alpha_4 \frac{[\text{C1}]^{\gamma_{\text{C1}}}}{\text{C1}_{50}^{\gamma_{\text{C1}}} + [\text{C1}]^{\gamma_{\text{C1}}}} [\text{pro-IL-1}\beta] - k_6 G [\text{IL-1}\beta_c] - \delta_2 [\text{IL-1}\beta_c], \quad (21)$$

$$\frac{d[\text{IL-1}\beta_e]}{dt} = k_6 G [\text{IL-1}\beta_c], \quad (22)$$

where $[\text{NF-}\kappa\text{B}_n]$ is defined in Equation (8) and G is a non-dimensionalised value that allows for [GSDMD-N]-dependent cytokine outflux, and water influx, such that,

$$G = G([\text{GSDMD-N}]) := \frac{[\text{GSDMD-N}]}{[\text{GSDMD}]+[\text{GSDMD-N}]} \quad (23)$$

IL-18: The above mechanisms are incorporated to describe the rate of change of [pro-IL-18], [IL-18_c] and [IL-18_e] over time as,

$$\frac{d[\text{pro-IL-18}]}{dt} = -\alpha_5 \frac{[\text{C1}]^{\gamma_{\text{C1}}}}{\text{C1}_{50}^{\gamma_{\text{C1}}} + [\text{C1}]^{\gamma_{\text{C1}}}} [\text{pro-IL-18}], \quad (24)$$

$$\frac{d[\text{IL-18}_c]}{dt} = \alpha_5 \frac{[\text{C1}]^{\gamma_{\text{C1}}}}{\text{C1}_{50}^{\gamma_{\text{C1}}} + [\text{C1}]^{\gamma_{\text{C1}}}} [\text{pro-IL-18}] - k_7 G [\text{IL-18}_c], \quad (25)$$

$$\frac{d[\text{IL-18}_e]}{dt} = k_7 G [\text{IL-18}_c]. \quad (26)$$

The levels of pro-IL-18 in the cell are kept at a homeostatic level [15, 18], therefore we include a conservation law,

$$[\text{pro-IL-18}] + [\text{IL-18}_c] + [\text{IL-18}_e] = \text{constant}. \quad (27)$$

2.7 Cell volume

The GSDMD-N derived membrane pores that allow for the outflux of mature interleukins, also allow for the influx of extracellular material (e.g., water). This influx causes the cell to swell until it eventually ruptures.

Single-cell analysis has revealed that before the ultimate membrane rupture occurs, the cell volume increases gradually [56]. Thus, in the model, we consider the volume of the cell, V , to increase at a rate k_8 once pores are formed on the cell membrane. We describe the rate of change of the cell volume by the equation,

$$\frac{dV}{dt} = k_8 G V. \quad (28)$$

Once the cell volume reaches a critical volume V_c , the cell ruptures and all cell processes cease.

2.8 Modified drug targeting model

We consider an anti-inflammatory drug (Drug) which binds to active NLRP3 and thus inhibits the inflammasome formation by preventing NLRP3-NLRP3 interactions. To incorporate this in our model, we consider the drug binding to NLRP3_a to form the complex Drug · NLRP3_a. The forward and reverse rate constants for this reaction are denoted by k_{+D} and k_{-D} , respectively. If we include these drug mechanisms in our model, Equation (6) describing the dynamics of NLRP3_a must be modified to include two additional terms,

$$\frac{d[\text{NLRP3}_a]}{dt} = \dots - k_{+D} [\text{Drug}] [\text{NLRP3}_a] + k_{-D} [\text{Drug} \cdot \text{NLRP3}_a]. \quad (29)$$

The rate of change of [Drug] and [Drug · NLRP3_a] can now be included in the model as,

$$\frac{d[\text{Drug}]}{dt} = -k_{+D} [\text{Drug}] [\text{NLRP3}_a] + k_{-D} [\text{Drug} \cdot \text{NLRP3}_a], \quad (30)$$

$$\frac{d[\text{Drug} \cdot \text{NLRP3}_a]}{dt} = k_{+D} [\text{Drug}] [\text{NLRP3}_a] - k_{-D} [\text{Drug} \cdot \text{NLRP3}_a], \quad (31)$$

where the following conservation law holds,

$$[\text{Drug}] + [\text{Drug} \cdot \text{NLRP3}_a] = \text{constant}. \quad (32)$$

2.9 Implementation of the pathway model

The model is implemented in MATLAB [57], where the system of ODEs (3)-(32) is solved numerically using the built-in ODE-solver `ode15s`. Model outputs are measured in terms of arbitrary units of concentration over time, or in units of volume over time. A more detailed description of the numerical set-up can be found in Appendix D, which also includes instructions on how to access and run the code. Simulation results are provided and discussed in the next section.

2.10 Results and discussion of the pathway model

We first consider the model without any drug, that is, we simulate the system given by Equations (3)-(28). Simulation results are provided in Figure 3, in which compound concentrations (in arbitrary units) and cell volume are plotted over time. We note that, [ASC_f], [pro-C1], [GSDMD] and [pro-IL-18] levels are not shown, however these concentrations can be directly obtained using the conservation laws detailed previously. The results show that NF- κ B is rapidly translocated to the nucleus upon DAMP/PAMP-induced TLR signalling. After [NF- κ B_n] levels have peaked, the transcription, and by extension the synthesis, of NLRP3_i and pro-IL-1 β is reduced as NF- κ B leaves the nucleus. Synthesised NLRP3_i activates to become NLRP3_a, which in turn oligomerises and binds together to form the inflammasome base, here expressed in terms of the concentration of NLRP3_o. These dynamics are captured in the subplot displaying the time evolution of [NLRP3_i], [NLRP3_a] and [NLRP3_o]. Note that once the inflammasome base is formed, the NLRP3_a-to-NLRP3_o oligomerisation plateaus and the binding of ASC to the inflammasome increases. This can be observed in the results, as [ASC_b] levels increase when [NLRP3_o] reaches the value n , where here $n \approx 1$. Furthermore, as [ASC_b] levels increase, the dimerisation and activation of caspase-1 is facilitated so

that $[C1]$ levels increase. In turn, when $[C1]$ levels increase, the cleavage of GSDMD, pro-IL-1 β and pro-IL-18 occurs. This is apparent in the subplots, as $[GSDMD-N]$, $[IL-1\beta_c]$ and $[IL-18_c]$ levels start increasing once $[C1]$ levels surpass zero. The outflux of mature interleukins and the influx of extracellular water to the cell is mediated by GSDMD-N derived pores, here implicitly modelled via the concentration $[GSDMD-N]$ using Equation (23). Thus, once GSDMD-N has been cleaved, so that $[GSDMD-N] > 0$, the cytoplasmic interleukin concentrations $[IL-1\beta_c]$ and $[IL-18_c]$ respectively decrease in favour of the extracellular concentrations $[IL-1\beta_e]$ and $[IL-18_e]$. $[GSDMD-N]$ levels over zero also enable the cellular volume to increase which eventually results in membrane rupture once the volume reaches the maximal capacity V_c , where here $V_c = 1.5$. Note that when membrane rupture occurs, all intracellular mechanisms are ceased and thus the time progression in the subplots stops.

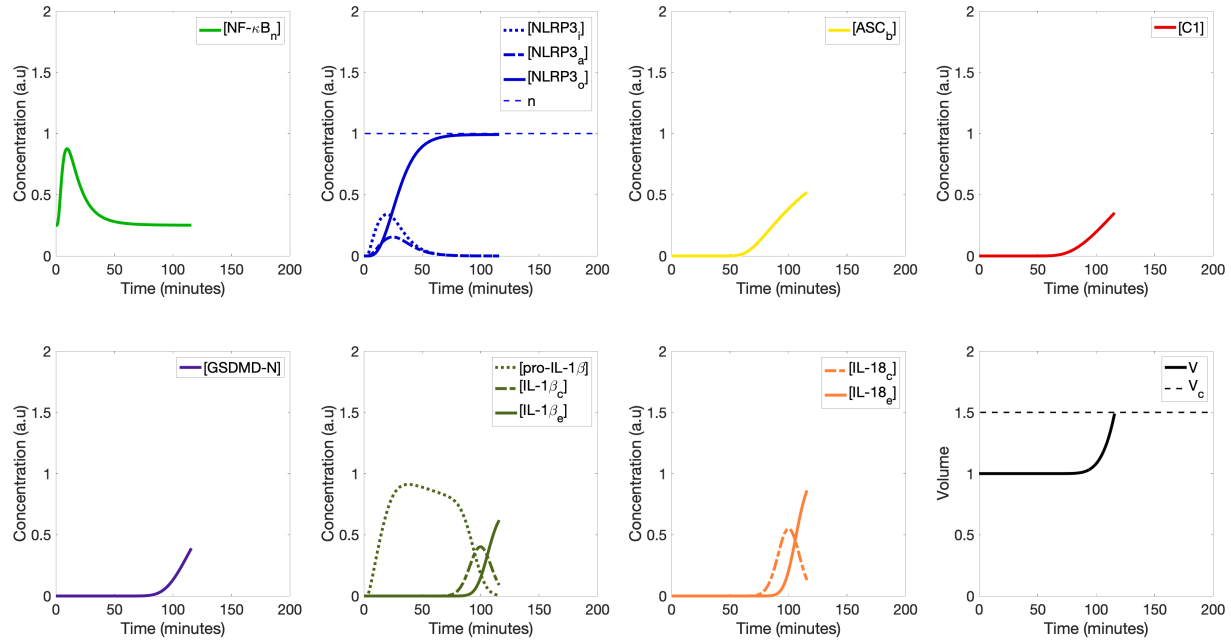


Figure 3. Numerical simulations results of the ODE model described by Equations (3)-(28) - that is, the model of pyroptosis in the absence of an anti-inflammatory drug. We display the concentration of each model component in arbitrary units (a.u) over time, as well as cell volume dynamics. Note that the time progression stops once the critical volume V_c is reached and the ultimate cell membrane rupture occurs.

We next consider numerical simulations of the model including the effects of an anti-inflammatory drug, that is the system given by Equations (3)-(28), with the modifications and additions described in Equations (29)-(31). The results of the numerical simulations are displayed in Figure 4, where we compare different initial concentrations (dosages) of the drug. We display the time evolution of each model component in a separate subplot, where the graph colour corresponds to drug dosage. These results show that increasing levels of the drug push pyroptotic events further in time. Note that the results for the maximal tested drug dosage results in many of the processes driving pyroptosis not occurring in the time frame examined. The drug specifically inhibits the NLRP3_a-to-NLRP3_o oligomerisation process. Therefore, when it is added to the system, we observe that as the drug concentration $[Drug]$ increases, so does the amount of time it takes for $[NLRP3_o]$ to reach the threshold value n . This means that the inflammasome base formation, and by extension the downstream processes resulting in inflammatory cytokine secretion and the ultimate membrane rupture, are delayed.

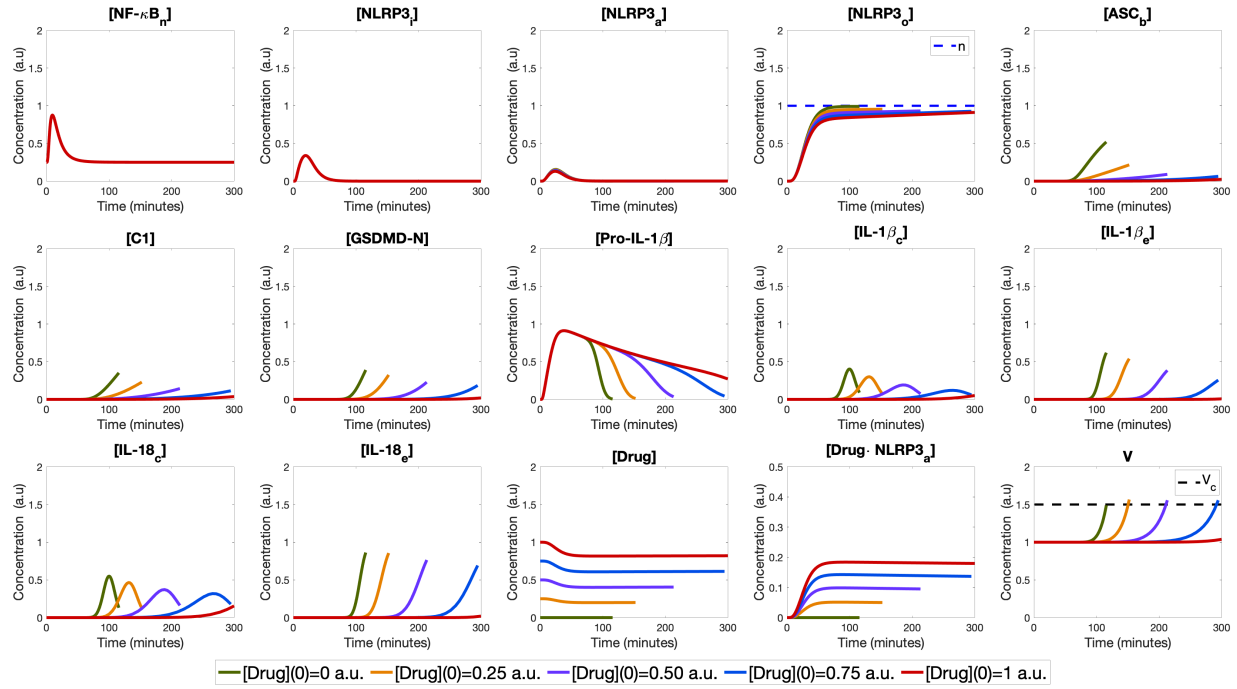


Figure 4. Numerical simulations results of the ODE model including an NLRP3-targeting anti-inflammatory drug, that is Equations (3)-(28) with Equations (29)-(31). We display the concentration of each model component in arbitrary units (a.u) over time, as well as cell volume dynamics for several dosages of the drug. The dynamics of each model component is plotted in a separate subplot, where the line colour corresponds to applied drug dosage, as described in the legend. Note that the time progression stops if the critical volume (*i.e.*, $V_c = 1.5$) is reached, as the cell membrane ruptures.

2.11 Sensitivity analyses of the pathway model

The mathematical model of the pyroptosis pathway includes a set of model parameters $\Theta = \{\theta_1, \theta_2, \dots, \theta_p\}$, which are listed in Table C.1 in Appendix C. As is further described in this Appendix, these model parameters have been collectively approximated through data fitting to time-course data available in the literature. We note that such a data fitting approach may lead to large parameter uncertainties and thus we conduct sensitivity analyses in order to investigate how sensitive the model output is to changes in the values of the model parameters Θ , hereby referred to as the model input. Such analyses can help us understand how changes in the model input can affect the model output [58, 59]. Therefore, this can allow us to identify which input parameters θ_j are the most influential, providing information on the importance of experimental retrieval of accurate parameters and possible model reductions. In this study we investigate the system of ODEs describing the pyroptosis pathway (Equations (3)-(28)), using three different sensitivity analysis techniques, namely robustness analysis (Section 2.11.1), Latin hypercube analysis (Section 2.11.2) and a derivative-based method (Section 2.11.3). The system of ODEs is summarised in System (33) in Appendix B, and we denote the computed compound concentrations over time as model outputs $y_i(t)$, where $i = 1, \dots, q$, as labelled in Table B.1.

2.11.1 Robustness analyses

Robustness analysis is a local sensitivity analysis technique in which one input parameter θ_j is varied, whilst the other $p - 1$ parameters are kept fixed at their estimated value [58, 59]. We compare the output compound concentrations $y_i(t)$ over time for, here 15, different perturbed values of each parameter θ_j . For brevity, in this section we include robustness analysis results for two input parameters, α_1 and α_2 , respectively denoting the rate coefficients for the transcription of inactive NLRP3 and the cleavage of GSDMD, in Figure 5. Further robustness analysis results for all input parameters $\theta_j, j = 1, \dots, 21$ are available in the Supporting Information (Supporting Information, S1). Figure 5 (top) shows that increasing α_1 speeds up the inflammasome base formation and, thereby, the pyroptosis process. For investigated values of α_1 below the threshold value $\alpha_1 = 0.06 \text{ (a.u) min}^{-1}$, the pyroptosis process is delayed to an extent that NLRP3 formation does not occur within the simulated 300 minutes. For the estimated values of the parameter set Θ , we consider such perturbations of α_1 to be unfeasible, since we are here aiming to simulate a scenario in which the NLRP3 inflammasome base is formed at around 77 minutes, and the ultimate membrane rupture occurs at 120 minutes, as is described in Appendix C. Figure 5 (bottom) shows that as α_2 increases, so does the concentration of GSDMD-N post-inflammasome formation, and thereby the ultimate membrane rupture gets pushed earlier in time. These results provide a visual overview of how increasing or decreasing each model parameter affects the output. Note that, apart from the NF- κ B translocation dynamics, all reactions in the model are irreversible, one-way reactions, as can be seen in Figure 1. This means that varying input parameters associated with NLRP3, ASC, caspase-1, GSDMD and cell volume dynamics will either speed up or slow down the pyroptosis process. Furthermore, varying parameters associated with the cytokines IL-1 β and IL-18 affects cytokine dynamics only.

2.11.2 Global sensitivity analysis

We perform a global sensitivity analysis, in which all parameters θ_j are simultaneously perturbed from their estimated values, using Latin hypercube sampling and analysis [58, 59]. Results from the Latin hypercube analysis are provided in the form of scatter plots, where the model outputs are plotted over chosen parameter ranges for each input parameter. Here the regarded output is the time-points for the ultimate membrane rupture. The scatter plots in Figure 6 provides a visual means to study the relationship between the input parameters and model outputs, for small perturbations (between $\pm 5\%$) of each input parameter θ_j . In order to quantify linear input-output associations, Figure 6 also includes Pearson correlation coefficients (R) for each input-output pair, evaluated over the regarded input parameter ranges [59]. A moderate negative linear input-output correlations ($R=-0.595$) is found for input parameter τ , implying that, given the estimated parameter values of Θ , our model results are especially sensitive to small perturbations of τ which influences the magnitude and duration of the nuclear NF- κ B peak. Weak positive linear input-output correlations are found for input parameters NF_{50} ($R=0.382$) and ν ($R=0.261$), also related to nuclear NF- κ B

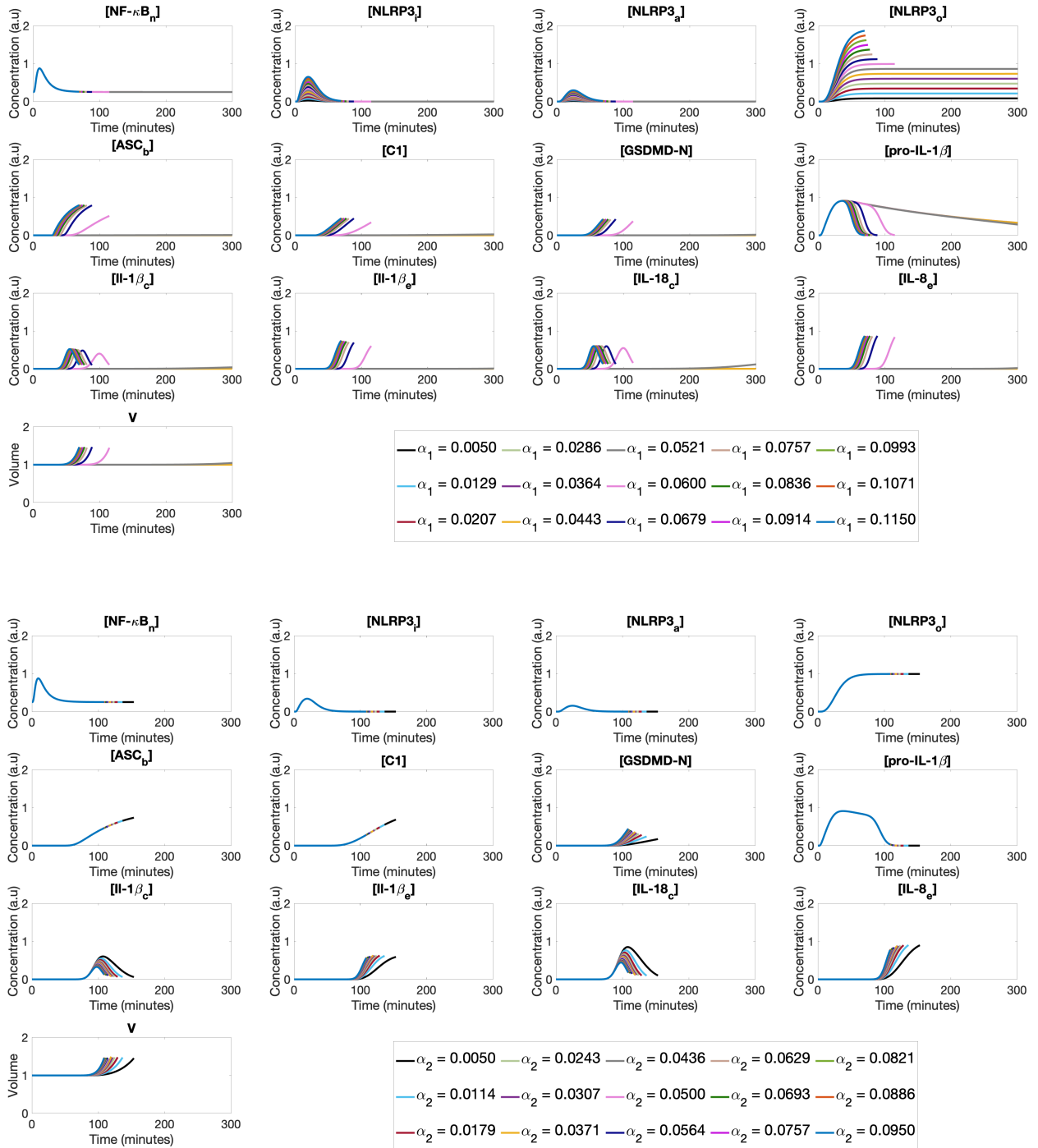


Figure 5. Robustness analyses. The plots show numerical simulations results of the ODE model, where the input parameters α_1 (top) and α_2 (bottom) are perturbed, one at a time, whilst other model parameters are fixed at their estimated values. Model components are measured in terms of arbitrary concentration units (a.u.) or volume. Note that the time progression stops once the critical volume V_c is reached and the ultimate cell membrane rupture occurs

dynamics. Note that model parameters describing cytokine dynamics do not affect the regarded outputs and are thus omitted from this global sensitivity analysis.

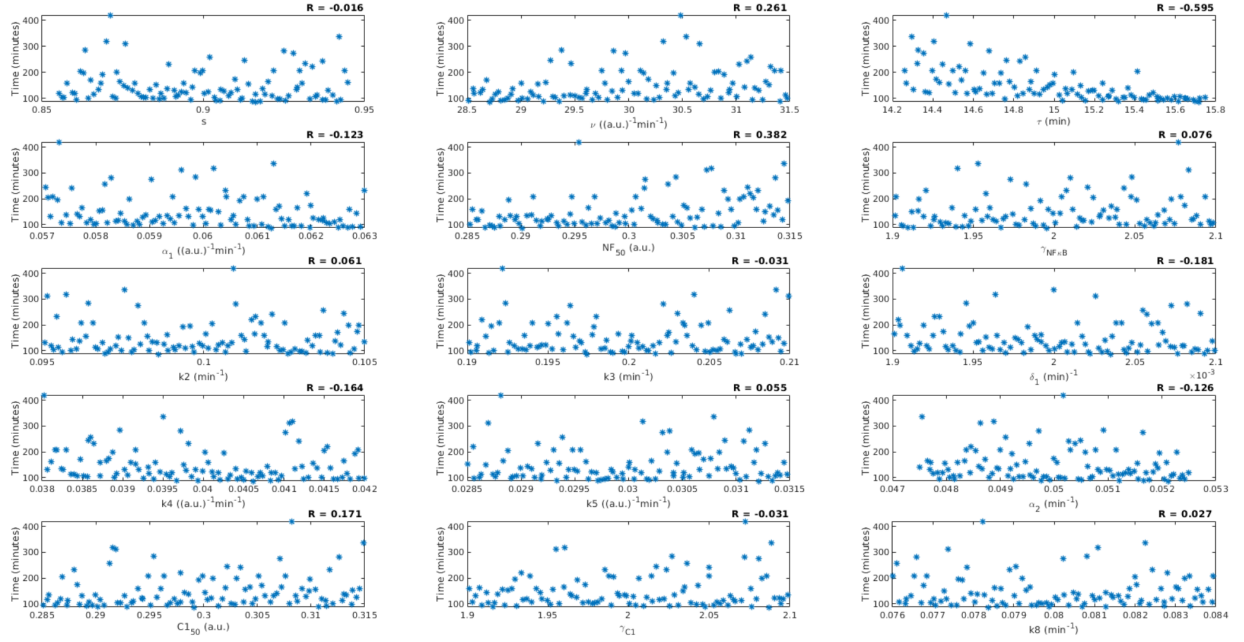


Figure 6. Global sensitivity analysis is performed using Latin hypercube sampling and analysis. The output, *i.e.*, the time-point of the ultimate membrane rupture, is plotted over various input parameters. Each input parameter range spans $\pm 5\%$ of the estimated parameter value. The Pearson correlation coefficient (R), measuring the linear association between each input-output pair, is provided at the top right corner of each corresponding subplot.

2.11.3 Derivative-based sensitivity analysis

We perform a derivative-based sensitivity analysis in which the equations describing the time evolution of the concentrations $y_i(t)$, where $i = 1, \dots, q$, are differentiated with respect to each input parameter θ_j where $j = 1, \dots, p$ [58, 60]. We thus compute $q \times p$ partial derivatives $z_j^i(t) = \partial y_i(t) / \partial \theta_j$, at each time-point t in which the system of ODEs is numerically solved. These partial derivatives $z_j^i(t)$ are also referred to as the model sensitivities and are here numerically computed using the Direct Method as described by Dickinson and Gelinas [60]. The values $z_j^i(t)$ provide time-varying measurements of the sensitivity of the outputs $y_i(t)$ with respect to changes in values of the input parameters θ_j . Results from the derivative-based sensitivity analysis for three input parameters α_1 , α_1 and α_1 are presented in Figure 7, in which sensitivities with respect to τ , s and ν , *i.e.*, z_τ^i , z_s^i and z_ν^i , are plotted over time. Results for sensitivities with respect to other model input parameters are available in the Supporting Information (Supporting Information, S2) which notably demonstrate that no output concentration $y_i(t)$ displays sensitivity to the decay constants δ_1 and δ_2 in the current model setup. Whereas, Figure 7 shows that, for the estimated parameter values of Θ , the concentration of NF- κ B is sensitive to small perturbations of τ , s and ν whilst nuclear NF- κ B concentrations are above the initial homeostatic NF- κ B concentration. As a downstream effect, the concentrations [NLRP3₁], [NLRP3_a], [NLRP3₀] and [pro-IL- β] are also sensitive to small perturbations of τ , s and ν , albeit to a lesser extent than [NF- κ B].

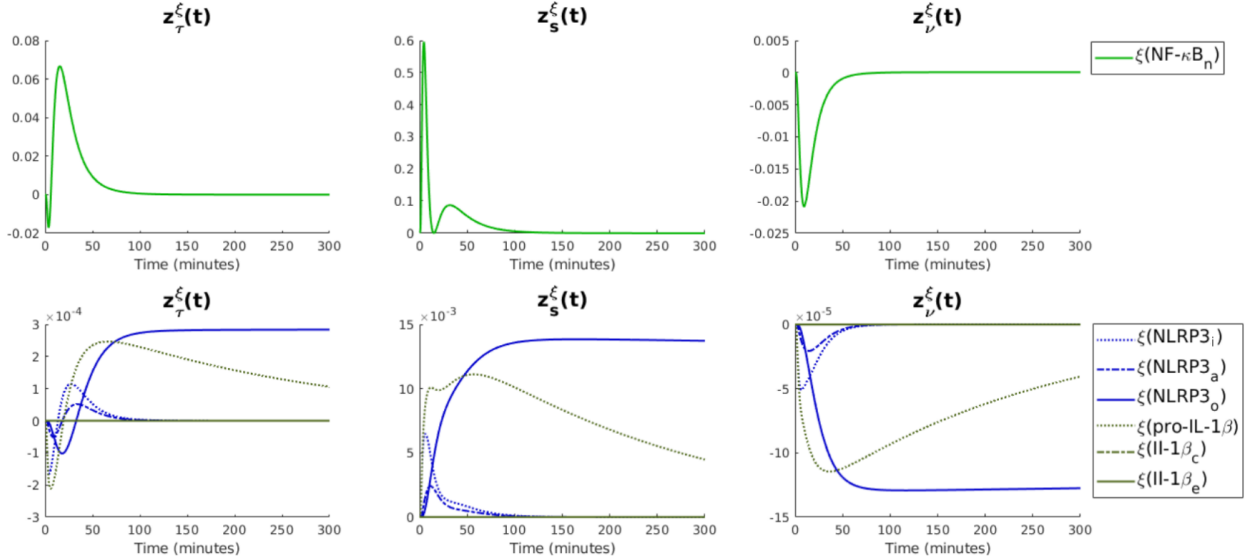


Figure 7. A derivative-based sensitivity analysis shows that (top) the output results describing NF- κ B concentrations over time are sensitive to small perturbations of the input parameters τ , s and ν , for the estimated parameter values of Θ . As a downstream effect, (bottom) NLRP3 and pro-IL-1 β output concentrations are also sensitive to small perturbations of τ , s and ν . Here z_j^i denotes the sensitivity of the output concentration computed in equation i , with respect to the input parameter θ_j , where $\xi(\text{compound name})$ maps each compound to its governing equation index i .

3 Integrating the pyroptosis pathway model with the PhysiCell framework

3.1 Overview

Our single-cell pyroptosis model described in Section 2, is currently being integrated within a multiscale tissue simulator developed to investigate within-host dynamics of SARS-CoV-2. This work is part of a multidisciplinary, international coalition led by Paul Macklin (Indiana University, USA). The coalition is made up of several subgroups who are developing individual submodels which are integrated to form a virtual lung epithelium implemented using PhysiCell, an open source physics-based cell simulator [61]. In the project, epithelial cells are modelled as susceptible to SARS-CoV-2 infection. Other cell types, such as immune cells, are also included in the model but are not susceptible to the virus.

The PhysiCell SARS-CoV-2 framework consists of a hybrid agent-based model that aims to capture; virus transmission in the tissue, intracellular viral processes (e.g., binding, endocytosis, replication, exocytosis), infected cell responses (e.g., metabolism, chemokine secretion, cell death via apoptosis, cell death via pyroptosis), immune cell dynamics (e.g., recruitment, activation, infiltration and predation of infected cells) and tissue damage due to infection and/or host response. For more detail on each model component, we refer the reader to the most recent preprint from the coalition [50]. In line with a rapid prototyping and open source research approach, the project has been through several versions and will be updated further as each submodel is refined. Here, we will give a brief overview of the hybrid framework and discuss some of the implications of pyroptosis in the PhysiCell tissue simulator, using the version 3 code, with our added pyroptosis model. The pyroptosis model is fully integrated into the version 4 code, which at the time of writing is not yet released.

3.2 Simulation outline and implementation

At the start of each PhysiCell SARS-CoV-2 tissue simulation, virions (virus particles) are non-uniformly distributed across the epithelial cells. Virions diffuse across the tissue and can be endocytosed via ACE-2 receptors, and thereafter replicated and released by epithelial cells. If the viral RNA in an epithelial cell surpasses a threshold value R_{RNA} , the epithelial cell undergoes pyroptosis with a probability $\Pi \in [0, 1]$, and apoptosis with a probability $1 - \Pi$. The intracellular pyroptosis model governs the cellular pyroptosis-induced secretion of the cytokines IL-18 and IL-1 β , as well as the increase in cytoplasmic volume due to water influx, and the ultimate cell membrane rupture.

Once secreted, extracellular IL-18 and IL-1 β are modelled as diffusible fields across the tissue. IL-1 β has been shown to cause a pyroptotic bystander effect, whereby increased IL-1 β levels can induce pyroptosis in uninfected, or infected, cells [19, 62–64]. Therefore, in the model, epithelial cells can internalise extracellular IL-1 β , and if the level of internalised IL-1 β surpasses a threshold value $R_{IL-1\beta}$, the pyroptosis cascade is initiated in the cell. Diffusion, secretion and uptake of virions and cytokines are handled by built-in PhysiCell functionalities, as is apoptosis. A modified version of the system of ODEs describing the pyroptosis pathway is numerically solved using the backward Euler method. Further details regarding implementation, as well as information on how to access the code, are provided in Appendix F.

3.3 Agent-based model results

We now utilise the PhysiCell SARS-CoV-2 Tissue simulator to investigate the effects of pyroptosis on a cellular-level scale. We design *in silico* experiments to study research questions related to virus-induced cell death. In these *in silico* experiments we investigate scenarios in which epithelial cells are exposed to virus in the absence of an immune system, simulating *in vitro* experiments. We investigate the impact of two key parameters, that are described above, $R_{IL-1\beta}$ and Π .

Simulation results are provided in form of cell maps and cell count data in Figures 8 and 9. In the cell maps provided throughout this section, epithelial cells are shown in blue when they are viable, *i.e.*, neither pyroptosing nor apoptosing. Uninfected epithelial cells are shown in an opaque colour, whilst infected epithelial cells are depicted with a transparency proportional to their viral load. Cells in which the pyroptosis process has been induced due to viral loads or bystander effects (IL-1 β levels) are respectively shown in orange and red. Once cell membrane rupture occurs, as determined by the intracellular pyroptosis pathway model, a pyroptosing cell is removed from the system. Apoptosing cells turn black and reduce in size until they are removed from the system. Note that, the cell count data is based on the number of cells of various phenotypes, present in the system over time, cells that have been removed from the system are not included in these counts. The data shown in the time-course plots are the average over 10 runs of the simulation, while the cell maps are chosen from one run of the simulations as an example. For all cases, the standard deviation between runs is very small, with the case depicted in Figure 9(B) being the most noticeable (*i.e.*, more variable). To ensure that this small variability is clear, we include a larger version of the time-course plot of Figure 9(B) in Appendix F, as seen in Figure F.2.

We first study the impact of the bystander effect of IL-1 β , where pyroptosis may be induced in infected or uninfected cells that are nearby pyroptosing cells secreting the cytokine. In Figure 8 we display the results corresponding to three values of the threshold, $R_{IL-1\beta}$, specifically (A) $R_{IL-1\beta} = 0.5R$, (B) $R_{IL-1\beta} = R$ and (C) $R_{IL-1\beta} = 1.5R$, where R_{est} denotes an chosen threshold concentration (in units of μM). Comparing the three cell map progressions, we observe that all cases, (A), (B) and (C), give similar results until the 24h time-point. The later cell maps, at the 30h time-point, highlight qualitative differences between the results of the three cases. At this time-point, when we have a lower threshold for the bystander effect, as seen in case (A), we observe a large number of pyroptosing cells (induced by the bystander effect) and fewer viable cells in the system in comparison to the other cases, (B) and (C). In the median case (B), there is some bystander effect occurring, however not to as large an extent as case (A). When we have a higher threshold for the bystander effect, as seen in case (C), we have very little bystander effect occurring at the 30h time-point. These qualitative differences are continued when comparing the 36h time-point, whereby a lower threshold for the bystander effect (case (A)), results in most of the epithelial cells being removed from the system, while a higher threshold (case (C)), results in a larger number of epithelial cells remaining.

When comparing the time-course plots, we see that there is a significant difference in height of the spike of cells induced through the bystander effect, where case (A) is largest and case (C) is smallest as expected. These results highlight that the IL-1 β threshold value required for pyroptosis affects the ratio of the method of pyroptosis induction (virus or IL-1 β), and also the time it takes for all cells to be removed from the system, as pyroptosis is a more rapid mode of cell death than apoptosis. Although the results from these simulations are qualitative, the model provides a framework in which to study bystander effects. Upon availability, data related to IL-1 β levels required for pyroptosis induction could be incorporated in the model for a more quantitative analysis.

We next study the impact of the probability that an infected cell undergoes pyroptosis as opposed to apoptosis, in response to viral load, as determined by the parameter Π . In Figure 9 we display the results corresponding to three values of Π . As before, comparing the three cell map progressions, we observe that all cases, (A), (B) and (C), give similar results until the 24h time-point. The qualitative differences between the three cases are clear when comparing the cell maps at the 36h time-point. In case (A) where the probability of pyroptosis is $\Pi = 0$, the results show that a large number of viable epithelial cells remain. However, in case (B) where $\Pi = 0.5$, by the 36hr time-point there are fewer viable cells remaining and more cells undergoing pyroptosis, mainly from the bystander effect. Finally, when $\Pi = 1$ in case (C), by the 36h time-point most of the viable epithelial cells have been removed, with some pyroptosing cells remaining. Through the time-course plots, we can see the clear distinction of cells undergoing apoptosis versus pyroptosis between the three cases. These simulation results show that increasing the value of Π speeds up the overall eradication of epithelial cells. The reason for this is two-fold: pyroptosis contributes to bystander induced cell deaths and the pyroptosis process is faster than apoptosis. More specifically, the time it takes for a cell to pyroptose or apoptose in the simulation is 2 and 8.5 hours respectively. We note, that in the time-course plot for case (B), where $\Pi = 0.5$, we observe a visible standard deviation resulting from 10 simulation runs. This is due to the added stochasticity in the model arising from the non-deterministic mode of cell death when $\Pi \neq 0$ and $\Pi \neq 1$. The time-course plot for $\Pi = 0.5$ is included in a zoomed-in format in Appendix F, Figure F.2.

4 Conclusions and future work

Pyroptosis has been identified as a key mechanism involved in the cytokine storm and the inflammation associated with severe cases of COVID-19 [2]. Consequently, pyroptosis has been suggested as a target pathway to treat symptoms of COVID-19. In order to investigate the pathway of pyroptosis in further detail, we formulate a single-cell mathematical model that captures the key proteins and intracellular processes involved in this pro-inflammatory mode of cell death. Specifically, we model the process from DAMP/PAMP-induced TLR signalling to membrane rupture and the resulting cell death. The model is described in terms of a system of ODEs describing the dynamics of protein concentrations and cell volume. We further expand the model to include pharmacodynamic effects of a generic, NLRP3-targeting anti-inflammatory drug, and then perform both local and global sensitivity analyses in order to investigate how sensitive the model results are to the model parameters and their estimated values. Finally, we provide some detail on how this single-cell model is being integrated into a wider cellular-scale model that is being used to investigate SARS-CoV-2 progression in lung epithelial cells.

Recently, it has been found that if the pyroptosis pathway is inhibited, a cell can undergo apoptosis instead, a form of non-inflammatory cell death [11, 16, 18, 21, 65]. In our single-cell model, described in Section 2, we have shown in our simulations that the inclusion of an NLRP3-targeting anti-inflammatory drug can delay the formation of the inflammasome, and therefore may provide a method of switching the cell death mode from inflammatory to non-inflammatory. The single-cell model developed in this study could further be extended to investigate more specific pharmacodynamic actions of anti-inflammatory drugs that target the formation of the NLRP3 inflammasome, a comprehensive review of such drugs is provided by Bertinara *et al.* [15]. One such drug is tranilast, an NLRP3-targeting drug that is traditionally used for treating inflammatory diseases, such as asthma, in Japan and South Korea. Tranilast is currently being re-purposed for treating COVID-19 related symptoms in a clinical trial¹ [2, 66]. Moreover, corticosteroids such as Dexamethasone have

¹Chinese Clinical Trial Registry, registration number: ChiCDrug2000030002.

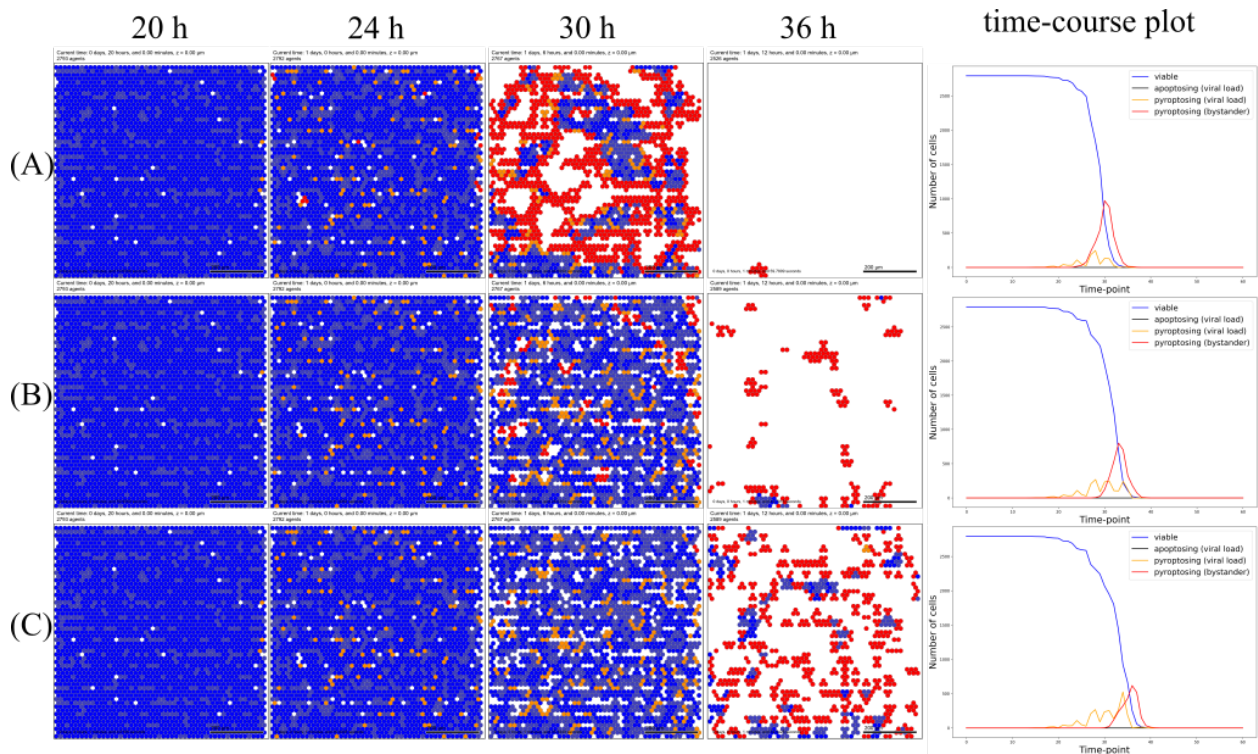


Figure 8. Cell map progressions and averaged time-course data for three situations, investigating the bystander effect of IL-1 β in the PhysiCell SARS-CoV-2 framework. We test three values for the threshold level of IL-1 β required to initiate pyroptosis: (A) $R_{IL-1\beta} = 0.5 R_{est}$, (B) $R_{IL-1\beta} = R_{est}$ and (C) $R_{IL-1\beta} = 1.5 R_{est}$, where R_{est} is a chosen base-line value. Viable cells (opaque blue), infected cells (less opaque blue), cells undergoing apoptosis (black), cells undergoing viral induced pyroptosis (orange) and cells undergoing bystander induced pyroptosis (red) are shown in the cell maps, and the corresponding cell counts at each time-point are displayed in the time-course plots. Note, here $\Pi = 1$.

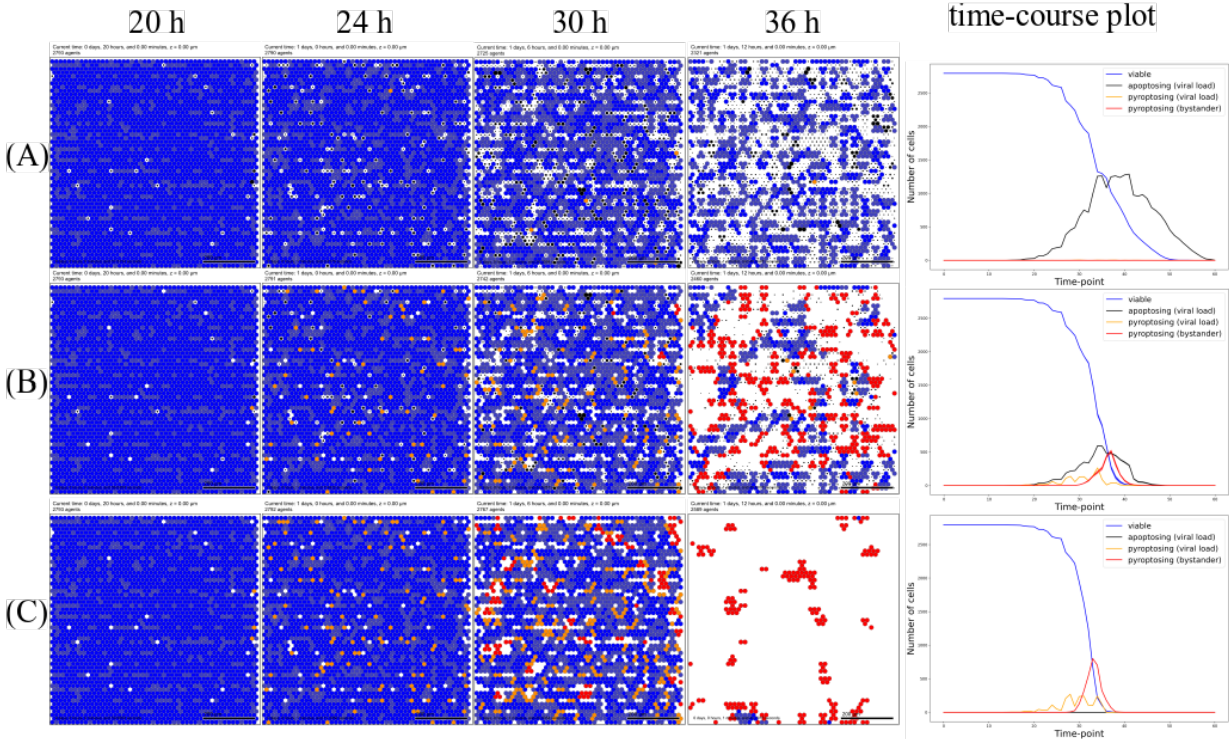


Figure 9. Cell map progressions and averaged time-course data for three situations, investigating the probability of a cell undergoing pyroptosis instead of apoptosis in response to viral load, Π , in the PhysiCell SARS-CoV-2 framework. We test three values: (A) $\Pi = 0$, (B) $\Pi = 0.5$ and (C) $\Pi = 1$. Viable cells (opaque blue), infected cells (less opaque blue), cells undergoing apoptosis (black), cells undergoing viral induced pyroptosis (orange) and cells undergoing bystander induced pyroptosis (red) are shown in the cell maps, and the corresponding cell counts at each time-point are displayed in the time-course plots. Note, here $R_{IL-1\beta} = R_{est}$, the baseline value.

been suggested as agents to counter the cytokine storm in severe cases of COVID-19 [67], and preliminary reports from clinical trials suggest that low-dose dexamethasone therapy has beneficial effects in COVID-19 patients requiring ventilation or supplemental oxygen [68]. As a corticosteroid, Dexamethasone has many potential pharmacodynamic effects. Of relevance to the study of pyroptosis is that Dexamethasone has been shown to directly bind to, or indirectly inhibit, NF- κ B, thus preventing the transcription of NLRP3 and pro-inflammatory cytokines [69]. Therefore, in future work, we could mathematically investigate the impact that this type of drug action would have on the single-cell pathway model.

When investigating the role of pyroptosis in the PhysiCell SARS-CoV-2 framework, as described in Section 3, our results highlight that the mode of cell death impacts the cellular-scale dynamics. In this paper we have investigated an *in vitro* situation, however the PhysiCell framework supports the inclusion of tissue-level components, such as immune cells and interferons (IFNs), to simulate *in vivo* scenarios. IFNs can play a role in inhibiting inflammasome activation and cytokine storms [2]. Type II IFNs typically affect the processes downstream of NLRP3 signalling [70], while type I IFNs regulate the upstream processes [71]. Moreover, the role of type I IFNs in the treatment of COVID-19 is being investigated [72]. Using the PhysiCell SARS-CoV-2 tissue simulator, we could investigate the effects of allowing IFNs to interact with the pyroptosis pathway. Furthermore, previous studies have shown that IL-18 can act as a recruiter of immune cells [19, 62, 73–76]. Therefore, in the PhysiCell SARS-CoV-2 framework, we are implementing processes that allow extracellular IL-18 to act as an immune-cell recruiting cytokine.

We finally remark that pyroptosis had been identified as a potential contributor to symptoms in various diseases other than COVID-19 [2], such as other virus-induced diseases [19], auto-immune diseases [15, 62] and cancer [17, 21, 77]. Therefore, the mathematical pyroptosis model developed in this paper could be modified and used to investigate the effect of pyroptosis in other disease scenarios.

Funding

SJH was supported by the Medical Research Council [grant code MR/R017506/1].

Acknowledgments

The authors would like to thank the SARS-CoV-2 Tissue Simulation Coalition for ongoing collaboration and feedback on model development. Further, this work is part of the RAMP (Rapid Assistance in Modelling the Pandemic) initiative, coordinated by the Royal Society, UK. The authors would like to thank Prof. Mark A.J. Chaplain (University of St Andrews) for coordinating our RAMP Task Team modelling within-host dynamics.

SARS-CoV-2 Tissue Simulation Coalition: <http://physicell.org/covid19/>.

RAMP: <https://royalsociety.org/topics-policy/health-and-wellbeing/ramp/>.

References

- [1] P. Zhou, X. Yang, X. Wang, B. Hu, L. Zhang, W. Zhang, H. Si, Y. Zhu, B. Li, C. Huang, et al. A pneumonia outbreak associated with a new coronavirus of probable bat origin. *Nature*, 579(7798):270–273, 2020.
- [2] J.K.Y. Yap, M. Moriyama, and A. Iwasaki. Inflammasomes and pyroptosis as therapeutic targets for COVID-19. *J. Immunol.*, page ji2000513, 2020.
- [3] M.Z. Tay, C.M. Poh, L. Rénia, P.A. MacAry, and L.F.P. Ng. The trinity of COVID-19: Immunity, inflammation and intervention. *Nat. Rev. Immunol.*, 20(6):363–374, 2020.

[4] M. Soy, G. Keser, P. Atagündüz, F. Tabak, I. Atagündüz, and S. Kayhan. Cytokine storm in COVID-19: Pathogenesis and overview of anti-inflammatory agents used in treatment. *Clin. Rheumatol.*, 39(7):2085–2094, 2020.

[5] D. Tang, P. Comish, and R. Kang. The hallmarks of COVID-19 disease. *PLoS Pathog.*, 16(5):e1008536, 2020.

[6] A. Shah. Novel coronavirus-induced NLRP3 inflammasome activation: A potential drug target in the treatment of COVID-19. *Front. Immunol.*, 11:1021, 2020.

[7] M.Z. Ratajczak and M. Kucia. SARS-CoV-2 infection and overactivation of NLRP3 inflammasome as a trigger of cytokine “storm” and risk factor for damage of hematopoietic stem cells. *Leukemia*, pages 1–4, 2020.

[8] Y. Fu, Y. Cheng, and Y. Wu. Understanding SARS-CoV-2-mediated inflammatory responses: From mechanisms to potential therapeutic tools. *Virol. Sin.*, pages 1–6, 2020.

[9] S. Nagashima, M.C. Mendes, A.P. Camargo, N.H. Borges, T.M. Godoy, A.F.R. Miggioro, F. da Silva Dezidério, C. Machado-Souza, and L. De Noronha. Endothelial dysfunction and thrombosis in patients with COVID-19—brief report. *Arterioscler. Thromb. Vasc. Biol.*, 40(10):2404–2407, 2020.

[10] Y. Jamilloux, T. Henry, A. Belot, S. Viel, M. Fauter, T. El Jammal, T. Walzer, B. François, and P. Sèvre. Should we stimulate or suppress immune responses in COVID-19? Cytokine and anti-cytokine interventions. *Autoimmun. Rev.*, 19(7):102567, 2020.

[11] C.Y. Taabazuing, M.C. Okondo, and D.A. Bachovchin. Pyroptosis and apoptosis pathways engage in bidirectional crosstalk in monocytes and macrophages. *Cell Chem. Biol.*, 24(4):507–514, 2017.

[12] N. Kelley, D. Jeltema, Y. Duan, and Y. He. The NLRP3 inflammasome: An overview of mechanisms of activation and regulation. *Int. J. Mol. Sci.*, 20(13):3328, 2019.

[13] P. Song, W. Li, J. Xie, Y. Hou, and C. You. Cytokine storm induced by SARS-CoV-2. *Clin. Chim. Acta*, 509:280–287, 2020.

[14] C. Huang, Y. Wang, X. Li, L. Ren, J. Zhao, Y. Hu, L. Zhang, G. Fan, J. Xu, X. Gu, et al. Clinical features of patients infected with 2019 novel coronavirus in Wuhan, China. *The Lancet*, 395(10223):497–506, 2020.

[15] M. Bertinaria, S. Gastaldi, E. Marini, and M. Giorgis. Development of covalent NLRP3 inflammasome inhibitors: Chemistry and biological activity. *Arch. Biochem. Biophys.*, 670:116–139, 2019.

[16] K. Tsuchiya. Inflammasome-associated cell death: Pyroptosis, apoptosis, and physiological implications. *Microbiol. Immunol.*, 64(4):252–269, 2020.

[17] S.L. Fink and B.T. Cookson. Apoptosis, pyroptosis, and necrosis: Mechanistic description of dead and dying eukaryotic cells. *Infect. Immun.*, 73(4):1907–1916, 2005.

[18] A.G. Kozloski. Inflammasome. *Mater. Methods*, 10:2869, 2020.

[19] A. Stutz, D.T. Golenbock, and E. Latz. Inflammasomes: Too big to miss. *J. Clin. Invest.*, 119(12):3502–3511, 2009.

[20] S. Christgen, D.E. Place, and T.D. Kanneganti. Toward targeting inflammasomes: Insights into their regulation and activation. *Cell Res.*, 30(4):315–327, 2020.

[21] Z. Zheng and G. Li. Mechanisms and therapeutic regulation of pyroptosis in inflammatory diseases and cancer. *Int. J. Mol. Sci.*, 21(4), 2020.

[22] M.G. Sanders, M.J. Parsons, A.G. Howard, J. Liu, S.R. Fassio, J.A. Martinez, and L. Bouchier-Hayes. Single-cell imaging of inflammatory caspase dimerization reveals differential recruitment to inflammasomes. *Cell Death Dis.*, 6:e1813, 2015.

[23] C. Semino, S. Carta, M. Gattorno, R. Sitia, and A. Rubartelli. Progressive waves of IL-1 β release by primary human monocytes via sequential activation of vesicular and gasdermin D-mediated secretory pathways. *Cell Death Dis.*, 9(11):1–14, 2018.

[24] G. Lopez-Castejon and D. Brough. Understanding the mechanism of IL-1 β secretion. *Cytokine Growth Factor Rev.*, 22(4):189–195, 2011.

[25] P. Broz, P. Pelegrín, and F. Shao. The gasdermins, a protein family executing cell death and inflammation. *Nat. Rev. Immunol.*, pages 1–15, 2019.

[26] L. DiPeso, D.X. Ji, R.E. Vance, and J.V. Price. Cell death and cell lysis are separable events during pyroptosis. *Cell Death Disc.*, 3(1):1–10, 2017.

[27] D. Brough and N.J. Rothwell. Caspase-1-dependent processing of pro-interleukin-1 β is cytosolic and precedes cell death. *J. Cell Sci.*, 120(5):772–781, 2007.

[28] K. Schleich and I.N. Lavrik. Mathematical modeling of apoptosis. *Cell Comm. Signal.*, 11(1):1–7, 2013.

[29] S.L. Spencer and P.K. Sorger. Measuring and modeling apoptosis in single cells. *Cell*, 144(6):926–939, 2011.

[30] W. Wang and T. Zhang. Caspase-1-mediated pyroptosis of the predominance for driving CD4 T cells death: A nonlocal spatial mathematical model. *Bull. Math. Biol.*, 80(3):540–582, 2018.

[31] D. Veltman, T. Laeremans, E. Passante, and H. J. Huber. Signal transduction analysis of the NLRP3-inflammasome pathway after cellular damage and its paracrine regulation. *J. Theor. Biol.*, 415:125–136, 2017.

[32] Y. Bozkurt, A. Demir, B. Erman, and A. Güll. Unified modeling of familial mediterranean fever and cryopyrin associated periodic syndromes. *Comp. Math. Meth. Med.*, page 893507, 2015.

[33] F. López-Caamal and H.J. Huber. Stable IL-1 β -activation in an inflammasome signalling model depends on positive and negative feedbacks and tight regulation of protein production. *IEEE ACM T. Comput. Bi.*, 16(2):627–637, 2018.

[34] WHO. World Health Organisation Statement on the Pandemic. <https://www.who.int/dg/speeches/detail/who-director-general-s-opening-remarks-at-the-media-briefing-on-covid-19—11-march-2020>, 2020.

[35] F. Akpinar, B. Inankur, and J. Yin. Spatial-temporal patterns of viral amplification and interference initiated by a single infected cell. *J. Virol.*, 90(16):7552–7566, 2016.

[36] A. Bankhead, E. Mancini, A.C. Sims, R.S. Baric, S. McWeeney, and P.M.A. Sloot. A simulation framework to investigate in vitro viral infection dynamics. *J. Comput. Sci.*, 4(3):127–134, 2013.

[37] A.L. Bauer, C. Beauchemin, and A.S. Perelson. Agent-based modeling of host-pathogen systems: The successes and challenges. *Inf. Sci.*, 179(10):1379–1389, 2009.

[38] G. Bocharov, A. Meyerhans, N. Bessonov, S. Trofimchuk, and V. Volpert. Spatiotemporal dynamics of virus infection spreading in tissues. *PLoS One*, 11(12):e0168576, 2016.

[39] C. Beauchemin, S. Forrest, and F. T. Koster. Modeling influenza viral dynamics in tissue. In *International Conference on Artificial Immune Systems*, pages 23–36. Springer, 2006.

[40] C. Beauchemin. Probing the effects of the well-mixed assumption on viral infection dynamics. *J. Theor. Biol.*, 242(2):464–477, 2006.

[41] C. Beauchemin, J. Samuel, and J. Tuszynski. A simple cellular automaton model for influenza A viral infections. *J. Theor. Biol.*, 232(2):223–234, 2005.

[42] D. Levin, S. Forrest, S. Banerjee, C. Clay, J. Cannon, M. Moses, and F. Koster. A spatial model of the efficiency of T cell search in the influenza-infected lung. *J. Theor. Biol.*, 398:52–63, 2016.

[43] N. Fachada, V.V. Lopes, and A. Rosa. Simulating antigenic drift and shift in influenza A. In *Proceedings of the 2009 ACM symposium on Applied Computing*, pages 2093–2100, 2009.

[44] A.L. Jenner, F. Frascoli, A.C.F. Coster, and P.S. Kim. Enhancing oncolytic virotherapy: Observations from a Voronoi cell-based model. *J. Theor. Biol.*, 485:110052, 2020.

[45] D. Wodarz, A. Hofacre, J.W. Lau, Z. Sun, H. Fan, and N.L. Komarova. Complex spatial dynamics of oncolytic viruses in vitro: Mathematical and experimental approaches. *PLoS Comput. Biol.*, 8(6):e1002547, 2012.

[46] G. An. Introduction of an agent-based multi-scale modular architecture for dynamic knowledge representation of acute inflammation. *Theor. Biol. Med.*, 5(1):11, 2008.

[47] R.C. Cockrell and G. An. Examining the controllability of sepsis using genetic algorithms on an agent-based model of systemic inflammation. *PLoS Comput. Biol.*, 14(2):e1005876, 2018.

[48] F. Fatehi, R.J. Bingham, E.C. Dykeman, P.G. Stockley, and R. Twarock. Comparing antiviral strategies against COVID-19 via multi-scale within host modelling. *ArXiv preprint ArXiv:2010.08957*, 2020.

[49] T.J. Sego, J.O. Aponte-Serrano, J.F. Gianlupi, S.R. Heaps, K. Breithaupt, L. Brusch, J. Crawshaw, J. M. Osborne, E.M. Quardokus, R.K. Plemper, et al. A modular framework for multiscale, multicellular, spatiotemporal modeling of acute primary viral infection and immune response in epithelial tissues and its application to drug therapy timing and effectiveness. *BioRxiv preprint BioRxiv:2020.04.27.064139*, 2020.

[50] Y. Wang, G. An, A. Becker, C. Cockrell, N. Collier, M. Craig, C.L. Davis, J. Faeder, A.N.F. Versypt, J.F. Gianlupi, et al. Rapid community-driven development of a SARS-CoV-2 tissue simulator. *BioRxiv preprint BioRxiv:2020.04.02.019075*, 2020.

[51] A.V. Bagaev, A.Y. Garaeva, E.S. Lebedeva, A.V. Pichugin, R.I. Ataullakhanov, and F.I. Ataullakhanov. Elevated pre-activation basal level of nuclear NF- κ B in native macrophages accelerates LPS-induced translocation of cytosolic NF- κ B into the cell nucleus. *Sci. Reports*, 9(1):1–16, 2019.

[52] C. Zhang, C. Zhao, X. Chen, R. Tao, S. Wang, G. Meng, X. Liu, C. Shao, and X. Su. Induction of ASC pyroptosis requires gasdermin D or caspase-1/11-dependent mediators and IFN β from pyroptotic macrophages. *Cell Death Dis.*, 11(6):470, 2020.

[53] Y. Huang, H. Jiang, and Y. et al. Chen. Tranilast directly targets NLRP3 to treat inflammasome-driven diseases. *EMBO Mol. Med.*, 10(4):e8689, 2018.

[54] M.S. Salahudeen and P.S. Nishtala. An overview of pharmacodynamic modelling, ligand-binding approach and its application in clinical practice. *Saudi Pharm. J.*, 25(2):165–175, 2017.

[55] A. Iliev, N. Kyurkchiev, and S. Markov. On the approximation of the step function by some sigmoid functions. *Math. Comput. Simul.*, 133:223 – 234, 2017.

[56] N.M. de Vasconcelos, N. Van Opdenbosch, H. Van Gorp, E. Parthoens, and M. Lamkanfi. Single-cell analysis of pyroptosis dynamics reveals conserved GSDMD-mediated subcellular events that precede plasma membrane rupture. *Cell Death Diff.*, 26(1):146–161, 2019.

[57] MATLAB. *version 1.8.0_202 (R2019n)*. The MathWorks Inc., Natick, Massachusetts, 2019.

[58] G. Qian and A. Mahdi. Sensitivity analysis methods in the biomedical sciences. *Math Biosci*, 2020.

[59] S. Hamis, S. Stratiev, and G.G. Powathil. Uncertainty and sensitivity analyses methods for agent-based mathematical models: An introductory review. *The Physics of Cancer: Research Advances*, ed. *Bernard Gerstman, Singapore: World Scientific Publishing.*, 2020.

[60] R.P. Dickinson and R.J. Gelinas. Sensitivity analysis of ordinary differential equation systems – a direct method. *Journal of Computational Physics*, 21(2):123 – 143, 1976.

[61] A. Ghaffarizadeh, R. Heiland, S.H. Friedman, S.M. Mumenthaler, and P. Macklin. PhysiCell: An open source physics-based cell simulator for 3-D multicellular systems. *PLoS Comput. Biol.*, 14(2):e1005991, 2018.

[62] T. Bergsbaken, S. L. Fink, and B. T. Cookson. Pyroptosis: Host cell death and inflammation. *Nat. Rev. Microbiol.*, 7(2):99–109, 2009.

[63] K. Lipinska, K.E. Malone, M. Moerland, and C. Kluft. Applying caspase-1 inhibitors for inflammasome assays in human whole blood. *J. Immunol. Meth.*, 411:66–69, 2014.

[64] K. Schroder and J. Tschopp. The inflammasomes. *Cell*, 140(6):821–832, 2010.

[65] W. He, H. Wan, L. Hu, P. Chen, X. Wang, Z. Huang, Z. Yang, C. Zhong, and J. Han. Gasdermin D is an executor of pyroptosis and required for interleukin-1 β secretion. *Cell Res.*, 25(12):1285–1298, 2015.

[66] M.P. Lythgoe and P. Middleton. Ongoing clinical trials for the management of the COVID-19 pandemic. *Trends Pharmacol. Sci.*, 41(6):363–382, 2020.

[67] K. Sharun, R. Tiwari, J. Dhama, and K. Dhama. Dexamethasone to combat cytokine storm in COVID-19: Clinical trials and preliminary evidence. *Int. J. Surg.*, 82:179–181, 2020.

[68] RECOVERY Collaborative Group. Dexamethasone in hospitalized patients with covid-19—Preliminary report. *N. Engl. J. Med.*, page 2021436, 2020.

[69] T. Rhen and J.A. Cidlowski. Antiinflammatory action of glucocorticoids—New mechanisms for old drugs. *N. Engl. J. Med.*, 353(16):1711–1723, 2005.

[70] B.B. Mishra, V.A.K. Rathinam, G.W. Martens, A.J. Martinot, H. Kornfeld, K.A. Fitzgerald, and C.M. Sassetti. Nitric oxide controls the immunopathology of tuberculosis by inhibiting NLRP3 inflammasome-dependent processing of IL-1 β . *Nature Immunol.*, 14(1):52–60, 2013.

[71] G. Guarda, M. Braun, F. Staehli, A. Tardivel, C. Mattmann, I. Förster, M. Farlik, T. Decker, R.A. Du Pasquier, P. Romero, et al. Type I interferon inhibits interleukin-1 production and inflammasome activation. *Immunity*, 34(2):213–223, 2011.

[72] K.G. Lokugamage, A. Hage, C. Schindewolf, R. Rajsbaum, and V.D. Menachery. SARS-CoV-2 is sensitive to type I interferon pretreatment. *BioRxiv preprint BioRxiv:2020.03.07.982264*, 2020.

[73] C.A. Dinarello. Immunological and inflammatory functions of the interleukin-1 family. *Annu. Rev. Immunol.*, 27:519–550, 2009.

[74] Y. He, H. Hara, and G. Núñez. Mechanism and regulation of NLRP3 inflammasome activation. *Trends Biochem. Sci.*, 41(12):1012–1021, 2016.

[75] Z.B. Zalinger, R. Elliott, and S.R. Weiss. Role of the inflammasome-related cytokines IL-1 and IL-18 during infection with murine coronavirus. *J. Neurovirol.*, 23(6):845–854, 2017.

[76] J.J. O’Shea, M. Gadina, Siegel R.M., and J. Farber. Cytokines. In *Rheumatology*, pages 99–112. 2015.

[77] S. Lee, M. Hirohama, M. Noguchi, K. Nagata, and A. Kawaguchi. Influenza A virus infection triggers pyroptosis and apoptosis of respiratory epithelial cells through the type I interferon signaling pathway in a mutually exclusive manner. *J. Virology*, 92(14), 2018.

[78] C. Juliana, T. Fernandes-Alnemri, S. Kang, A. Farias, F. Qin, and E.S. Alnemri. Non-transcriptional priming and deubiquitination regulate NLRP3 inflammasome activation. *J. Biol. Chem.*, 287(43):36617–36622, 2012.

[79] J.S. Lolkema and D. Slotboom. The Hill analysis and co-ion–driven transporter kinetics. *J. Gen. Physio.*, 145(6):565–574, 2015.

[80] S. Han, T.B. Lear, J.A. Jerome, S. Rajbhandari, C.A. Snavely, D.L. Gulick, K.F. Gibson, C. Zou, B. B. Chen, and R.K. Mallampalli. Lipopolysaccharide primes the NALP3 inflammasome by inhibiting its ubiquitination and degradation mediated by the SCFFBXL2 E3 ligase. *J. Bio. Chem.*, 290(29):18124–18133, 2015.

[81] M.A. Moors and S.B. Mizel. Proteasome-mediated regulation of interleukin-1 β turnover and export in human monocytes. *J. Leukocyte Biol.*, 68(1):131–136, 2000.

[82] F. Martín-Sánchez, C. Diamond, M. Zeitler, A.I. Gomez, A. Baroja-Mazo, J. Bagnall, D. Spiller, M. White, M.J.D. Daniels, A. Mortellaro, et al. Inflammasome-dependent IL-1 β release depends upon membrane permeabilisation. *Cell Death Diff.*, 23(7):1219–1231, 2016.

A Abbreviations used in text

- ARDS: acute respiratory distress syndrome
- ASC: apoptosis-associated speck-like protein containing a CARD
- CARD: caspase activation and recruitment domain
- COVID-19: coronavirus disease 2019
- CD: Catalytic domain
- C1-CD: the catalytic domain of caspase-1
- DAMP: damage associated molecular pattern
- GSDMD: gasdermin D
- GSDMD-N: N-terminal domain of GSDMD
- IFN: interferon
- IL-1 β : interleukin 1 β
- IL-18: interleukin 18
- LLR: leucine-rich repeat
- NBD: nucleotide-binding and oligomerisation domain
- NF- κ B: nuclear factor kappa-light-chain-enhancer of activated B cells
- NLRP3: NBD, LRR-containing receptors with an N-terminal PYD 3
- ODE: ordinary differential equation
- PAMP: pathogen associated molecular pattern
- pro-IL-1 β : pro-form of interleukin 1 β
- pro-IL-18: pro-form of interleukin 18
- PYD: pyrin domain
- SARS-CoV-2: severe acute respiratory syndrome coronavirus 2
- TLR: toll like receptor

B Detailed model description and motivation

In this appendix we provide further details of the modelling terms chosen within our single-cell pathway model described in Section 2, we additionally provide the full model as ODE System (33). Model variables/components are listed in Table B.1 and the model parameters are discussed in Appendix C.

Label	Symbol	Component Description
y_1	$[\text{NF-}\kappa\text{B}_n](t)$	concentration of nuclear NF- κ B
y_2	$[\text{NLRP3}_i](t)$	concentration of inactive NLRP3 protein
y_3	$[\text{NLRP3}_a](t)$	concentration of active NLRP3 protein
y_4	$[\text{NLRP3}_o](t)$	concentration of oligomerised NLRP3 protein
y_5	$[\text{ASC}_f](t)$	concentration of free cytosolic ASC protein
y_6	$[\text{ASC}_b](t)$	concentration of bound ASC protein
y_7	$[\text{pro-C1}](t)$	concentration of pro-caspase-1
y_8	$[\text{C1}](t)$	concentration of activated caspase-1
y_9	$[\text{GSDMD}](t)$	concentration of inactive GSDMD
y_{10}	$[\text{GSDMD-N}](t)$	concentration of activated GSDMD-N
y_{11}	$[\text{pro-IL-1}\beta](t)$	concentration of pro-IL-1 β
y_{12}	$[\text{IL-1}\beta_c](t)$	concentration of active IL-1 β in the cytoplasm
y_{13}	$[\text{IL-1}\beta_e](t)$	concentration of active IL-1 β external
y_{14}	$[\text{pro-IL-18}](t)$	concentration of pro-IL-18
y_{15}	$[\text{IL-18}_c](t)$	concentration of active IL-18 in the cytoplasm
y_{16}	$[\text{IL-18}_e](t)$	concentration of active IL-18 external
y_{17}	$V(t)$	cell volume
y_{18}	$[\text{Drug}](t)$	concentration of free anti-inflammatory drug
y_{19}	$[\text{Drug} \cdot \text{NLRP3}_a](t)$	concentration of anti-inflammatory drug - NLRP3 _a complex

Table B.1. The symbols and descriptions of the components considered in the model. The bracket notation [] denotes compound concentration. Implicit time-dependence is denoted by (t).

B.1 Full system of ODEs for the single-cell pathway model

$$\begin{aligned}
\frac{d[\text{NF-}\kappa\text{B}_n]}{dt} &= -S_1 \cdot \frac{1}{t^2 s \nu} (2 \log(t) + s) e^{-\frac{\log^2 t}{s}}, \\
\frac{d[\text{NLRP3}_i]}{dt} &= \alpha_1 \frac{[[\text{NF-}\kappa\text{B}_n](t) - [\text{NF-}\kappa\text{B}_n](0)]^{\gamma_{\text{NF}}}}{\text{NF}_{50}^{\gamma_{\text{NF}}} + [[\text{NF-}\kappa\text{B}_n](t) - [\text{NF-}\kappa\text{B}_n](0)]^{\gamma_{\text{NF}}}} \\
&\quad - S_2 k_2 [\text{NLRP3}_i] - \delta_1 [\text{NLRP3}_i], \\
\frac{d[\text{NLRP3}_a]}{dt} &= S_2 k_2 [\text{NLRP3}_i] - k_3 [\text{NLRP3}_a] - \delta_1 [\text{NLRP3}_a] \\
&\quad - k_{+D} [\text{Drug}] [\text{NLRP3}_a] + k_{-D} [\text{Drug} \cdot \text{NLRP3}_a], \\
\frac{d[\text{NLRP3}_o]}{dt} &= k_3 [\text{NLRP3}_a], \\
\frac{d[\text{ASC}_f]}{dt} &= -k_4 \frac{1}{1 + \left(\frac{[\text{NLRP3}_o] - a}{b}\right)^{-c}} [\text{NLRP3}_o] [\text{ASC}_f], \\
\frac{d[\text{ASC}_b]}{dt} &= k_4 \frac{1}{1 + \left(\frac{[\text{NLRP3}_o] - a}{b}\right)^{-c}} [\text{NLRP3}_o] [\text{ASC}_f], \\
\frac{d[\text{pro-C1}]}{dt} &= -k_5 [\text{ASC}_b] [\text{pro-C1}], \\
\frac{d[\text{C1}]}{dt} &= k_5 [\text{ASC}_b] [\text{pro-C1}], \\
\frac{d[\text{pro-IL-1}\beta]}{dt} &= \alpha_3 \frac{[[\text{NF-}\kappa\text{B}_n](t) - [\text{NF-}\kappa\text{B}_n](0)]^{\gamma_{\text{NF}}}}{\text{NF}_{50}^{\gamma_{\text{NF}}} + [[\text{NF-}\kappa\text{B}_n](t) - [\text{NF-}\kappa\text{B}_n](0)]^{\gamma_{\text{NF}}}} \\
&\quad - \alpha_4 \frac{[\text{C1}]^{\gamma_{\text{C1}}}}{\text{C1}_{50}^{\gamma_{\text{C1}}} + [\text{C1}]^{\gamma_{\text{C1}}}} [\text{pro-IL-1}\beta] - \delta_2 [\text{pro-IL-1}\beta], \\
\frac{d[\text{IL-1}\beta_c]}{dt} &= \alpha_4 \frac{[\text{C1}]^{\gamma_{\text{C1}}}}{\text{C1}_{50}^{\gamma_{\text{C1}}} + [\text{C1}]^{\gamma_{\text{C1}}}} [\text{pro-IL-1}\beta] \\
&\quad - k_6 \frac{[\text{GSDMD-N}]}{[\text{GSDMD}] + [\text{GSDMD-N}]} [\text{IL-1}\beta_c] - \delta_2 [\text{IL-1}\beta_c], \\
\frac{d[\text{IL-1}\beta_e]}{dt} &= k_6 \frac{[\text{GSDMD-N}]}{[\text{GSDMD}] + [\text{GSDMD-N}]} [\text{IL-1}\beta_c], \\
\frac{d[\text{pro-IL-18}]}{dt} &= -\alpha_5 \frac{[\text{C1}]^{\gamma_{\text{C1}}}}{\text{C1}_{50}^{\gamma_{\text{C1}}} + [\text{C1}]^{\gamma_{\text{C1}}}} [\text{pro-IL-18}], \\
\frac{d[\text{IL-18}_c]}{dt} &= \alpha_5 \frac{[\text{C1}]^{\gamma_{\text{C1}}}}{\text{C1}_{50}^{\gamma_{\text{C1}}} + [\text{C1}]^{\gamma_{\text{C1}}}} [\text{pro-IL-18}] - k_7 \frac{[\text{GSDMD-N}]}{[\text{GSDMD}] + [\text{GSDMD-N}]} [\text{IL-18}_c], \\
\frac{d[\text{IL-18}_e]}{dt} &= k_7 \frac{[\text{GSDMD-N}]}{[\text{GSDMD}] + [\text{GSDMD-N}]} [\text{IL-18}_c], \\
\frac{dV}{dt} &= k_8 \frac{[\text{GSDMD-N}]}{[\text{GSDMD}] + [\text{GSDMD-N}]} V, \\
\frac{d[\text{Drug}]}{dt} &= -k_{+D} [\text{Drug}] [\text{NLRP3}_a] + k_{-D} [\text{Drug} \cdot \text{NLRP3}_a], \\
\frac{d[\text{Drug} \cdot \text{NLRP3}_a]}{dt} &= k_{+D} [\text{Drug}] [\text{NLRP3}_a] - k_{-D} [\text{Drug} \cdot \text{NLRP3}_a].
\end{aligned} \tag{33}$$

B.2 Signal 1.

The initial signal, S_1 , as defined in Equation (4), is here considered to be either *on*, $S_1 = 1$, or *off*, $S_1 = 0$. This binary choice is motivated by the modelling assumption that there will be no inflammasome-inducing

signalling until the DAMP/PAMP-sensing TLR activity is high enough. Therefore any signal level below some threshold value, here *e.g.*, $S_1 = 1$, would not stimulate a downstream response. We here also assumed that once S_1 is turned *on*, this signal is kept at a constant level until the cell dies. In future model adaptations this binary and constant signalling can be modified to allow for continuous responses determined by internal and external stimuli.

B.3 Signal 2.

In the model we assume that the second signal, S_2 , is either *on* or *off*. For all shown simulation results, we assume that S_2 is *on*, so that $S_2 = 1$, for all time-points in the simulation. Through experiments, Juliana *et al.* [78] showed that increasing the time that a cell was exposed to ATP (yielding a second signal S_2 to turn *on*) did not alter the subsequent inflammasome dynamics or the expression of involved proteins. Thus, it could be argued that assuming that S_2 is constant, *i.e.*, *on* or *off*, throughout the simulation is a reasonable model assumption.

B.4 Reaction terms.

To describe the transcription or cleavage terms we use a Hill function [54], of the form,

$$\alpha \frac{[A]^\gamma}{A_{50}^\gamma + [A]^\gamma}. \quad (34)$$

Here, A_{50} represents the level of $[A]$ required for the Hill function to reach the value of a half, often referred to the half-max value of $[A]$ [79]. Here, α is some rate parameter that determines how quickly the transcription or cleavage process occurs. To describe the activation terms in the ODE system we consider chemical reactions of the form,



where A and B are the inactive and active components, respectively. The reaction rate k determines how fast this process occurs. Using the law of mass action we can then translate this into the term used in the ODE for concentration $[A]$, *i.e.*, $-k[A][B]$, and for concentration $[B]$, *i.e.*, $+k[A][B]$.

Similarly, to include decay terms, we consider a chemical reaction of the form,



where \emptyset here denotes that the component is removed from the system. Again, using the law of mass action we can then use this to write the decay terms within the ODE for concentration $[A]$, *i.e.*, $-\delta[A]$. Binding interactions within the model are added considering a reaction of the form,



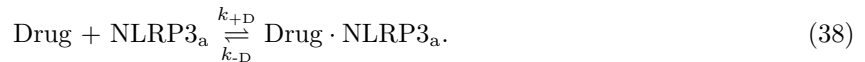
Here, component A and B bind together to form a 3rd component C and this process can use up (or not use up) component B . Using the law of mass action we can then use this to write the binding terms within the ODE for concentration $[A]$, *i.e.*, $-k[A][B]$, and concentration $[C]$, *i.e.*, $+k[A][B]$. Note, the terms for concentration $[B]$ will either be $-k[A][B]$ or will not be included, if the component is used up in the binding process or not, respectively.

B.5 Anti-inflammatory drug terms.

The influence of the anti-inflammatory drug is included in a modified version of the model which results in additional terms for the dynamics of NLRP3_a given in Equation (29). Also included in the drug model is the dynamics of the anti-inflammatory drug, Drug, and the complex Drug · NLRP3_a, as is in Equations (30) and (31). Here, we consider a binding reaction of the form,

Symbol	Description	Value
a	sigmoid constant for step-function approximation	1 (a.u.)
$\theta_1=\alpha_1$	transcription rate of NLRP3	0.06 (a.u.) min^{-1}
$\theta_2=\alpha_2$	cleavage rate of GDSMD	0.05 min^{-1}
$\theta_3=\alpha_3$	transcription rate of pro-IL-1 β	0.06 (a.u.) min^{-1}
$\theta_4=\alpha_4$	cleavage rate of pro-IL-1 β	0.5 min^{-1}
$\theta_5=\alpha_5$	cleavage rate of pro-IL-18	0.5 min^{-1}
b	sigmoid constant for step-function approximation	2 (a.u.)
c	sigmoid constant for step-function approximation	1000
$\theta_6=C1_{50}$	half-max value of caspase-1 required for cleavage	0.3 a.u.
$\theta_7=\delta_1$	decay rate of NLRP3	0.002 min^{-1}
$\theta_8=\delta_2$	decay rate of pro-IL-1 β and IL-1 β	0.004 min^{-1}
$\theta_9=\gamma_{\text{C1}}$	Hill function coefficient of caspase-1 mediated cleavage	2
$\theta_{10}=\gamma_{\text{NF}}$	Hill function coefficient of NF- κ B mediated transcription	2
$\theta_{11}=k_2$	activation rate of NLRP3	0.1 min^{-1}
$\theta_{12}=k_3$	oligomerisation rate of NLRP3	0.2 min^{-1}
$\theta_{13}=k_4$	rate for NLRP3 - ASC interaction	0.04 (a.u.) $^{-1}$ min^{-1}
$\theta_{14}=k_5$	rate for ASC - (pro-caspase-1) interactions	0.03 (a.u.) $^{-1}$ min^{-1}
$\theta_{15}=k_6$	transport rate of IL-1 β out of cell	0.5 min^{-1}
$\theta_{16}=k_7$	transport rate of IL-18 out of cell	0.5 min^{-1}
$\theta_{17}=k_8$	rate at which cell volume increases	0.08 min^{-1}
k_{+D}	forward rate constant for the drug-NLRP3 _a reaction	0.05 (a.u.) $^{-1}$ min^{-1}
k_{-D}	reverse rate constant for the drug-NLRP3 _a reaction	0.0005 min^{-1}
n	relative level of NLRP3 _o required for the inflammasome base	1 a.u.
$\theta_{18}=\text{NF}_{50}$	half-max value of NF- κ B required for transcription	0.3 a.u.
$\theta_{19}=s$	scaling parameter for NF- κ B dynamics	0.9
$\theta_{20}=\nu$	scaling parameter for NF- κ B dynamics	30
$\theta_{21}=\tau$	time-scaling parameter for NF- κ B dynamics	15 min
V_c	critical volume at which cell ruptures	1.5 a.u.

Table C.1. Parameters values used within numerical simulations of the model. The justification for these values is given in Appendix C. Here ‘a.u.’ refers to arbitrary units of concentration or volume. In the sensitivity analyses, we refer to these parameters as the input parameters $\Theta = \{\theta_1, \theta_2, \dots, \theta_p\}$.



Mass action kinetics allows us to write this interaction in terms of ODEs. We consider the anti-inflammatory drug to be a covalent inhibitor, and thus we could add an extra step in the above reaction. However, in lieu of relevant data, we are currently considering only one reaction step for Drug binding to NLRP3_o in an effort to not include extra model parameters.

C Model parameter values

In this appendix, we provide further detail on how we estimated the values of the parameters used within the single-cell pathway model simulations. The parameters used to perform numerical simulations of the model are those provided in Table C.1, unless stated otherwise.

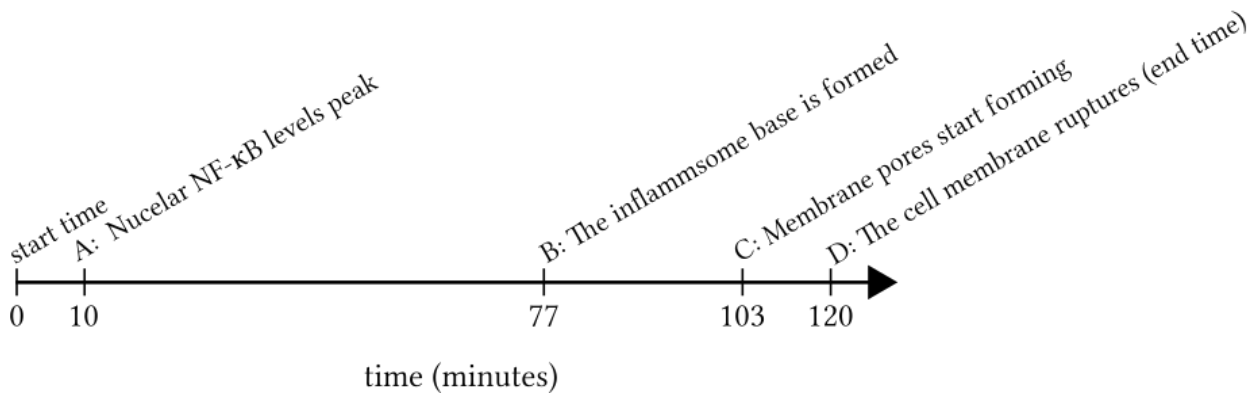


Figure C.1. We construct a timeline for the pyroptosis pathway using data from Bagaev *et al.* [51], de Vasconcelos *et al.* [56] and Martín-Sánchez *et al.* [82]. At 0 minutes (start time), Signal 1 (S_1) turns *on*. Thereafter, at 10 minutes, nuclear NF- κ B levels peak, after which the cytoplasmic-to-nuclear translocation of NF- κ B ceases in the mathematical model. 77 minutes into the timeline, enough NLRP3 has been transcribed, synthesised and activated to form the inflammasome base. Then, at 107 minutes, the GSDMD-N induced pores start forming, allowing the outflux of IL-1 β and IL-18, as well as the influx of extracellular water which causes the cell volume to start increasing. Finally, at 120 minutes (the end time) the cell membrane completely ruptures. At this point, around 90% of the pro-IL-1 β and pro-IL-18 will have been cleaved and subsequently released to the extracellular environment.

C.1 Decay parameters.

In [80], it was found that NLRP3 had a half-life of approximately 6 hrs when stimulated with lipopolysaccharide (LPS), which translates to a decay rate of approximately $0.002 \mu\text{m min}^{-1}$. Therefore we choose,

$$\delta_1 = 0.002 \text{ min}^{-1},$$

as we assume measure concentrations as dimensionless, arbitrary units. In [81], it was found that pro-IL-1 β had a half-life of approximately 2.5 hrs, which translates to a decay rate of approximately $0.004 \mu\text{m min}^{-1}$. Therefore we choose,

$$\delta_2 = 0.004 \text{ min}^{-1},$$

as we assume measure concentrations as dimensionless, arbitrary units.

C.2 The timeline of pyroptosis.

We use data from three experimental studies [51, 56, 82] to estimate a timeline for events regarded in our mathematical model. The values of the model parameters $\alpha_1 - \alpha_5$, C_{150} , γ_{C1} , γ_{NF} , k_{1a} , k_{1b} , $k_2 - k_8$, NF- κ B and V_c are chosen to obtain model dynamics that follow this experimentally motivated timeline of events **A-D**, which is illustrated in Figure C.1. Further detail of constructing this timeline is provided in the following paragraphs.

Bagaev *et al.* [51] studied NF- κ B kinetics in primary macrophages subjected to bacterial lipopolysaccharide (LPS). de Vasconcelos *et al.* [56] investigated subcellular key events that define pyroptosis using single-cell analysis. In their article, the authors provide a multitude of data pertaining to bone marrow-derived macrophages (BMDMs) that undergo caspase-1-dependent pyroptosis upon *Bacillus anthracis* lethal toxin (LeTx) stimulation. Martín-Sánchez *et al.* [82] measured the levels of pro-IL-1 β and external IL-1 β over time after inflammasome activation in systems with mouse BMDMs.

A: Bagaev *et al.* [51] reported that the nuclear NF- κ B concentration peaked at 10 minutes post LPS activation, after which it decreased to a half-maximal level in a gradual manner over 100 minutes.

B: de Vasconcelos *et al.* [56] showed that the influx of Ca^{2+} occurs before total membrane permeabilisation in pyroptosis (see Figure 7 in de Vasconcelos *et al.* [56]). Further data from their study suggests that changes in mitochondrial activity occur between (45+12=56) and (21+9=30) minutes prior to complete membrane rupture (see Figure 1 combined with Figure 3, as well as Supplementary Figure 3 in de Vasconcelos *et al.* [56]). If we assume that Ca^{2+} influx and changes in mitochondrial activity commence between the priming and activation events, we can estimate that the NLRP3 inflammasome base is formed somewhere between 56 to 30 minutes prior to cell rupture. In the model we use the average value (43 minutes) as the time before cell rupture (end time) when the inflammasome forms (*i.e.* when the concentration of NLRP3_o reaches the threshold value n). Therefore event **B** occurs around end time - 43 minutes = (120-43) minutes = 77 minutes.

C: In de Vasconcelos *et al.*'s study, cell volumes increase gradually for approximately 13 minutes prior to membrane rupture. Furthermore, cell volumes were reported to increase by approximately 50%. (See Figure 6a,b in de Vasconcelos *et al.* [56]).

D: Supernatants from cell cultures were assayed for LDH activity in de Vasconcelos *et al.*'s study. LDH is a cytosolic protein that is released by pyroptotic cells, and LDH activity is commonly used as a marker for plasma rupture in experimental settings. Data showed that near-maximal supernatant LDH values were reached 120 minutes post LeTx stimulation (see Figure 9c in de Vasconcelos *et al.* [56]). From this we approximate the time between signal 1 turning *on* in the model, and complete membrane rupture, to be approximately 120 minutes.

Furthermore, results from Martín-Sánchez *et al.*'s [82] study highlight that the release of $\text{IL-1}\beta$ coincided with membrane permeability (the formation of GSDMD-N derived membrane pores), and that eventually all of the pro- $\text{IL-1}\beta$ present at the start of the experiments was cleaved and released from the cell, with approximately 90% released within 120 minutes.

C.3 Anti-inflammatory drug parameters.

We consider drug concentrations to be constant during the simulated time span, effectively describing an *in vitro* scenario without drug wash out. This could be altered to include drug dosages varying in time if appropriate. Tranilast and oridonin examples of anti-inflammatory drugs that can inhibit the formation of the NLRP3 inflammasome by binding to active NLRP3 [15]. Therefore, to parameterise the model we consider data on this drug with the desired action. Immunoblot data presented by Huang *et al.* [53], pertaining to LPS-primed bone marrow derived macrophages (BMDMs) treated with tranilast, demonstrate dose-dependent (25-100 μM) drug responses, where the maximal inhibition was reached at 100 μM of the drug. With this motivation, we investigate drug dosages in increments of 0.25 (here arbitrary concentration units) and adjust the k_{-D}/k_{+D} ratio to be “completely effective” at 1 a.u.. At this stage in the model development, we interpret this “completely effectiveness” as the membrane rupture being delayed so that it does not occur within 300 simulated minutes. Accordingly, we set $k_{-D}/k_{+D} = 0.01\text{a.u.}$

D MATLAB code and set up of numerical simulations for the single-cell model

The single-cell mathematical model was implemented in MATLAB using the ODE solver `ode15s`. We solve the system of equations with the initial conditions (ICs),

$$[\text{NF-}\kappa\text{B}_n](0) = 0.25, \\ [\text{ASC}_f](0) = [\text{pro-C1}](0) = [\text{GSDMD}](0) = [\text{pro-IL-18}](0) = V(0) = 1,$$

while all other variables start out with a zero initial condition, to represent a cell in homeostasis. For the results shown in Figure 3 we consider the model without drug intervention, that is,

$$[\text{Drug}](0) = 0,$$

whereas, in the results shown in Figure 4 we consider the initial concentration of the drug to be a value between 0 and 1. Note, as we consider an *in vitro* situation we consider the drug to be present from the start of the simulations and not decay within the simulation time. The initial conditions pertaining to NF- κ B are motivated by previous experiments by Bagaev *et al.* [51], reporting initial nuclear NF- κ B concentrations to be between 10% and 30% (of the total amount of cellular NF- κ B), depending on cell line. For other variables with a non-zero IC, we set the value 1 to be the initial concentration as we are currently working with arbitrary units of concentration/volume and considering relative compound concentrations using the conservation laws provided throughout the manuscript.

The simulation results provided in Figures 3 and 4 are obtained by running the code with the ICs described above, along with the parameters given in Table C.1 and the signals S_1 and S_2 turned *on*. The MATLAB code, including user instructions, is available on our project GitHub page: <https://github.com/Pyroptosis>.

E Further details of the sensitivity analysis

The key outputs of our model are whether the inflammasome is formed, the levels of IL-1 β and IL-18 released into the external environment and the time it takes for the cell to rupture. We summarise the sensitivity analysis results in regards to the key outputs of the model in Table E.1. The plotted results for each robustness analysis can be found in Supporting Information, S1.

Parameter	Base formed	IL-1 β released	IL-18 released	Rupture time
$\alpha_1=0.005-0.11$	Prevented \rightarrow Faster	Prevented \rightarrow Faster	Prevented \rightarrow Faster	Prevented \rightarrow Faster
$\alpha_2=0.01-0.1$	-	Slower	Slower	Slower
$\alpha_3=0.005-0.11$	-	Increase	-	-
$\alpha_4=0.05-0.95$	-	Increase	-	-
$\alpha_5=0.05-0.95$	-	-	Increase	-
$C_{150}=0.05-0.55$	-	Slower	Slower	Slower
$\delta_1=0.0005-0.0035$	Slightly Slower	Slower	Slower	Slower
$\delta_2=0.001-0.007$	-	Decrease	-	-
$\gamma_{C1}=0.5-3.5$	-	Slower	Slower	Slower
$\gamma_{NF}=0.5-3.5$	Slightly Faster	Slower	Slower	Slower
$k_2=0.01-0.19$	Prevented \rightarrow Faster	Prevented \rightarrow Faster	Prevented \rightarrow Faster	Prevented \rightarrow Faster
$k_3=0.05-0.35$	Faster	Faster	Faster	Faster
$k_4=0.005-0.08$	-	Faster	Faster	Faster
$k_5=0.005-0.06$	-	Faster	Faster	Faster
$k_6=0.05-0.95$	-	Increase	-	-
$k_7=0.05-0.95$	-	-	Increase	-
$k_8=0.01-0.1$	-	Decrease	Decrease	Faster
$NF_{50}=0.05-0.55$	Slower \rightarrow Prevented	Slower \rightarrow Prevented	Slower \rightarrow Prevented	Slower \rightarrow Prevented
$s=0.1-1.7$	Prevented \rightarrow Faster	Prevented \rightarrow Faster	Prevented \rightarrow Faster	Prevented \rightarrow Faster
$\nu=15-45$	Slower \rightarrow Prevented	Slower \rightarrow Prevented	Slower \rightarrow Prevented	Slower \rightarrow Prevented
$\tau=5-25$	Prevented \rightarrow Faster	Prevented \rightarrow Faster	Prevented \rightarrow Faster	Prevented \rightarrow Faster

Table E.1. Robustness analysis results for each parameter tested, where resulting changes are correlated with the parameter values from the lowest value tested to the highest value tested. Here, ‘-’ denotes that there is no change in this result while varying the parameter. Those with ‘ \rightarrow ’ are cases in which the resulting qualitative dynamics change, (*i.e.*, there can be cases in which the inflammasome does not form).

F Reduced model and details of PhysiCell implementation

To implement the ODE pathway model, as described in Section 2, into the PhysiCell framework, the model must be discretised using the Backward Euler method. For Version 4 of the PhysiCell model, we use a reduced

version of our ODE model. In this reduced version the dynamics of NF- κ B are more linear. Furthermore, determining whether the inflammasome base has formed to allow ASC binding is determined by a binary on-off function, rather than the continuous form used previously. This function F is defined as,

$$F = F([\text{NLRP3}_o]) := \begin{cases} 1 & \text{if } [\text{NLRP3}_o] < n, \\ 0 & \text{if } [\text{NLRP3}_o] = n. \end{cases} \quad (39)$$

For the model we further utilise the conservation laws, for ASC (Equation (13)), Caspase-1 (Equation (16)), GSDMD (Equation (19)) and IL-18 (Equation (27)) where we set the constant to equal 1. This results in the system,

$$\begin{aligned} \frac{d[\text{NF-}\kappa\text{B}_n]}{dt} &= S_1 F k_{1a} (1 - [\text{NF-}\kappa\text{B}_n]) - k_{1b} [\text{NF-}\kappa\text{B}_n], \\ \frac{d[\text{NLRP3}_i]}{dt} &= \alpha_1 \frac{[\text{NF-}\kappa\text{B}_n]^{\gamma_{NF}}}{\text{NF}_{50}^{\gamma_{NF}} + [\text{NF-}\kappa\text{B}_n]^{\gamma_{NF}}} - S_2 k_2 [\text{NLRP3}_i] - \delta_1 [\text{NLRP3}_i], \\ \frac{d[\text{NLRP3}_a]}{dt} &= S_2 k_2 [\text{NLRP3}_i] - k_3 F [\text{NLRP3}_a] - \delta_1 [\text{NLRP3}_a], \\ \frac{d[\text{NLRP3}_o]}{dt} &= k_3 F [\text{NLRP3}_a], \\ \frac{d[\text{ASC}_b]}{dt} &= k_4 (1 - F) [\text{NLRP3}_o] (1 - [\text{ASC}_b]), \\ \frac{d[\text{C1}]}{dt} &= k_5 [\text{ASC}_b] (1 - [\text{C1}]), \\ \frac{d[\text{GSDMD-N}]}{dt} &= \alpha_2 \frac{[\text{C1}]^{\gamma_{C1}}}{\text{C1}_{50}^{\gamma_{C1}} + [\text{C1}]^{\gamma_{C1}}} (1 - [\text{GSDMD-N}]), \\ \frac{d[\text{pro-IL-1}\beta]}{dt} &= \alpha_3 \frac{[\text{NF-}\kappa\text{B}_n]^{\gamma_{NF}}}{\text{NF}_{50}^{\gamma_{NF}} + [\text{NF-}\kappa\text{B}_n]^{\gamma_{NF}}} - \alpha_4 \frac{[\text{C1}]^{\gamma_{C1}}}{\text{C1}_{50}^{\gamma_{C1}} + [\text{C1}]^{\gamma_{C1}}} [\text{pro-IL-1}\beta] - \delta_2 [\text{pro-IL-1}\beta], \\ \frac{d[\text{IL-1}\beta_c]}{dt} &= \alpha_4 \frac{[\text{C1}]^{\gamma_{C1}}}{\text{C1}_{50}^{\gamma_{C1}} + [\text{C1}]^{\gamma_{C1}}} [\text{pro-IL-1}\beta] - k_6 G [\text{IL-1}\beta_c] - \delta_2 [\text{IL-1}\beta_c], \\ \frac{d[\text{IL-1}\beta_e]}{dt} &= k_6 G [\text{IL-1}\beta_c], \\ \frac{d[\text{IL-18}_c]}{dt} &= \alpha_5 \frac{[\text{C1}]^{\gamma_{C1}}}{\text{C1}_{50}^{\gamma_{C1}} + [\text{C1}]^{\gamma_{C1}}} (1 - [\text{IL-18}_c] - [\text{IL-18}_e]) - k_7 G [\text{IL-18}_c], \\ \frac{d[\text{IL-18}_e]}{dt} &= k_7 G [\text{IL-18}_c], \\ \frac{dV}{dt} &= k_8 G V. \end{aligned} \quad (40)$$

We then discretise this using the Backward Euler method to implement it in to the ABM framework. The parameter values used are displayed in Table F.1 and we plot the solutions of the Backward Euler method using these parameters in Figure F.1. For more details of the full PhysiCell model we refer the reader to the current preprint [50] or the SARS-CoV-2 Tissue Simulation Coalition webpage: <http://physicell.org/covid19/>.

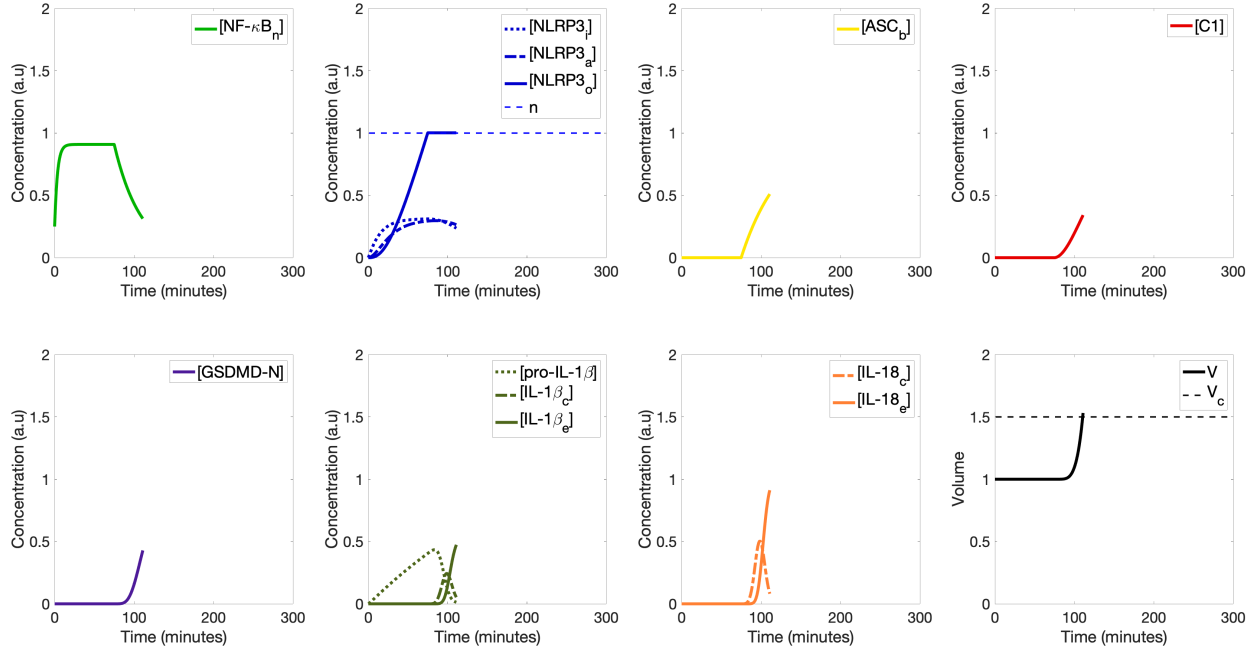


Figure F.1. Numerical simulations results of the Backward Euler discretisation of the ODE model described by Equation (39) and system of Equations (40) used within the PhysiCell framework. The parameters used are those displayed in Table F.1, which are chosen so that the key events occur at the same time as the results shown in Figure 3. We display the concentration of each model component in arbitrary units (a.u) over time, as well as cell volume dynamics. Note that the time progression stops once the critical volume V_c is reached and the ultimate cell membrane rupture occurs.

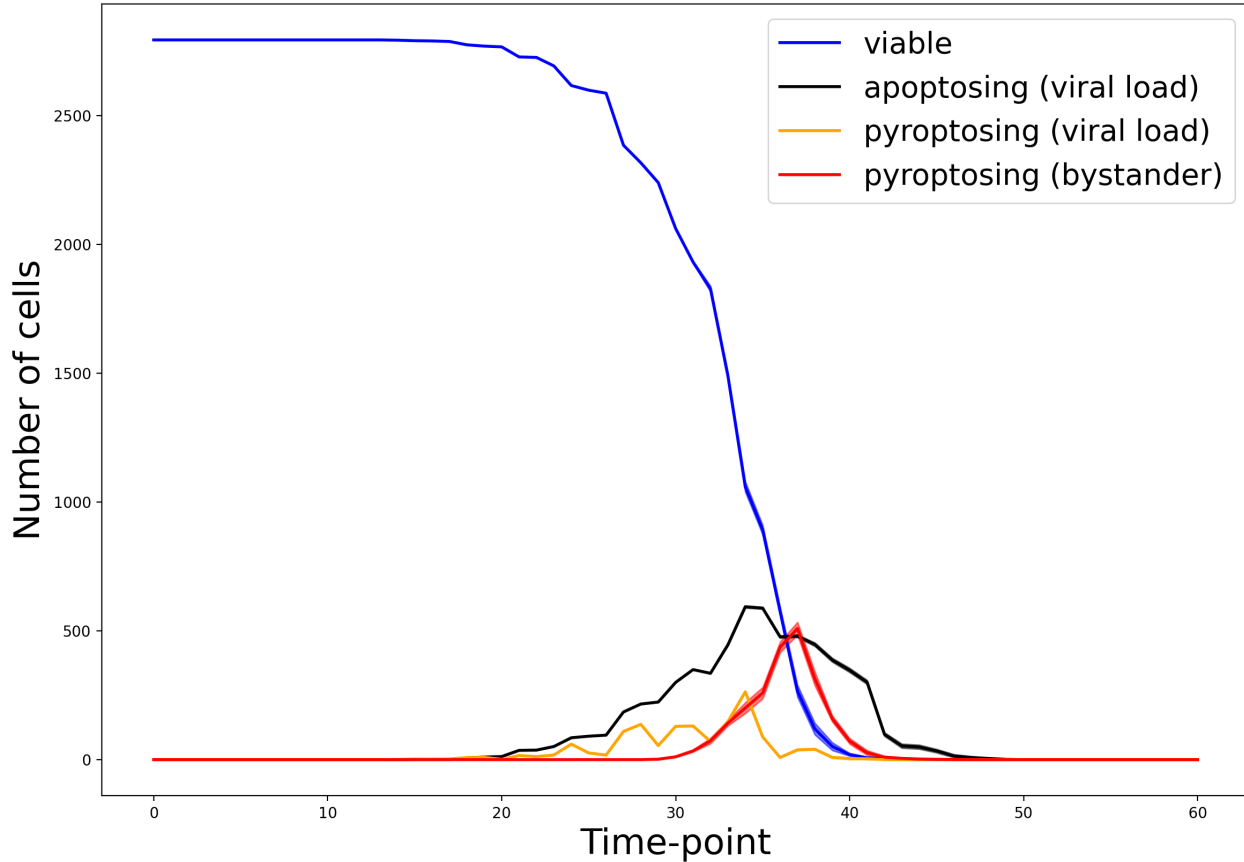


Figure F.2. The averaged time-course data for case from Figure 9(B), $R_{IL-1\beta} = R_{est}$ and $\Pi = 1$. Viable cells (blue), cells undergoing apoptosis (black), cells undergoing viral induced pyroptosis (orange) and cells undergoing bystander induced pyroptosis (red) are shown in the plots. The average over 10 runs is plotted as an opaque line, with the standard deviation filled in either side of the line in a more transparent line of the same colour.

Symbol	Description	Value
α_1	transcription rate of NLRP3	0.025 (a.u.) min^{-1}
α_2	cleavage rate of GDSMD	0.08 min^{-1}
α_3	transcription rate of pro-IL-1 β	0.007 (a.u.) min^{-1}
α_4	cleavage rate of pro-IL-1 β	0.8 min^{-1}
α_5	cleavage rate of pro-IL-18	0.8 min^{-1}
C_{150}	half-max value of caspase-1 required for cleavage	0.3 a.u.
δ_1	decay rate of NLRP3	0.002 min^{-1}
δ_2	decay rate of pro-IL-1 β and IL-1 β	0.004 min^{-1}
γ_{C1}	Hill function coefficient of caspase-1 mediated cleavage	2
γ_{NF}	Hill function coefficient of NF- κ B mediated transcription	2
k_{1a}	rate at which NF- κ B enters nucleus	0.3 min^{-1}
k_{1b}	rate at which NF- κ B leaves nucleus	0.03 min^{-1}
k_2	activation rate of NLRP3	0.07 min^{-1}
k_3	oligomerisation rate of NLRP3	0.07 min^{-1}
k_4	rate for NLRP3 - ASC interaction	0.02 (a.u.) $^{-1}$ min^{-1}
k_5	rate for ASC - (pro-caspase-1) interactions	0.04 (a.u.) $^{-1}$ min^{-1}
k_6	transport rate of IL-1 β out of cell	0.8 min^{-1}
k_7	transport rate of IL-18 out of cell	0.8 min^{-1}
k_8	rate at which cell volume increases	0.1 min^{-1}
n	relative level of NLRP3 _o required for the inflammasome base	1 a.u.
NF_{50}	half-max value of NF- κ B required for transcription	0.3 a.u.
V_c	critical volume at which cell ruptures	1.5 a.u.
Π	probability that cell will undergo pyroptosis vs apoptosis	0.5
R_{RNA}	threshold levels of viral RNA required to be detected	$1 - (1 \times 10^{-16})$
R_{est}	base threshold level of IL-1 β required to initiate pyroptosis	100

Table F.1. Parameters values used for the modified PhysiCell model described by Equation (39) and the ODE System(40). Here ‘a.u.’ refers to arbitrary units of concentration or volume. The relevant, additional parameters used for the integration with the agent-based model are also displayed.